Delft University of Technology

Thesis Report

Improving Frequency Targeting of Transmon Qubits Through Automated Laser Annealing

Authors:
BSc. Sean van der Meer

Supervisor:
Ir. N. Muthusubramanian
Prof. Dr. L. DiCarlo

October 8, 2021

TU Delft Delft University of Technology
QuTech
Casimir research school

Contents

1 Introduction

Quantum computing is a consequence of the ever increasing demand to tackle complex problems, while drastically reducing the computation time compared to classical computers. Algorithms have been proposed that emphasize the advantages of incorporating quantum mechanics to solve problems ranging from cryptography [1], material-science simulations to computational speedups [2–4]. As numerous as there are applications for quantum computing, so varied are the physical systems used to realize a controllable quantum system. Currently the most promising amongst the industry leading players are superconducting qubits [5, 6]. Besides mimicking the monolithic fabrication process from the semiconductor industry, superconducting qubits demonstrate fast and high-fidelity single and two-qubit gates which convincingly fulfill DiVincenzo's criteria as a prominent candidate for building a quantum computer [7]. However, decoherence errors arising in physical qubits due to undesirable interactions with their environment continues to limit the development of practical applications using few-qubit systems. This therefore necessitates the current research and development of two-dimensional lattice networks of physical qubits to implement surface codes in order to encode a logical qubit. A logical qubit is the abstraction of an ensemble of physical qubits which can be subject to unitary transformations and is more resilient to decoherence-induced errors. By interpreting the higher dimensional system of quantum information as a 2-D subspace in a logical qubit, one can create redundancy within the stored information. Such a logical qubit is considered fault-tolerant if the rate of errors accumulating within the physical qubit quantum state is less than the rate in detection and correction of said errors. [8–10].

For the research field of circuit quantum electrodynamics (cQED), which utilizes frequency-multiplexing, individual qubit frequencies need to be sufficiently distinguishable to reduce unwanted idle crosstalk between neighboring qubits [11]. Crosstalk is a widely used term from classical electronics that refers to unintended signal interactions between different parts of a circuit. In quantum computing experiments, residual ZZ-crosstalk[1] is defined as undesired dynamics that violate locality [12], where locality means that correlation between qubits can only be established through entangling gates and not through idle interactions between the higher levels of qubits coupled to a superconducting bus resonator [13, 14]. Crosstalk has been targeted as a significant contributor to the dephasing of logical qubits [11]. Most of these challenges related to frequency targeting can be addressed at the device fabrication step. From a development standpoint, device fabrication encapsulates: design, production, characterization and post-selection.

This thesis introduces a post-processing step that utilizes laser annealing as a precision tool to improve frequency targeting. Laser-based thermal annealing has been demonstrated in prior works as a facile and minimally invasive technique which causes a monotonic increase in junction resistance proportional to increasing annealing power density and duration. By thermally annealing a Josephson junction, the tunnel barrier thickness effectively increases [5, 15–17]. The objective is to design a closed-loop system that is able to automatically measure and anneal Al-AlOx Josephson junctions in order to improve the frequency targeting of transmon devices.

[1] The QuSurf architecture defines two forms of idle crosstalk, residual ZZ-interactions between nearest-neighbor qubits and residual exchange interactions (XX + YY) between next-nearest-neighbor same-frequency qubits.

1.1 Thesis Overview

This thesis is intended as a final update on the *LasiQ* Master thesis project and is submitted in partial fulfilment of the requirements for the degree of Master of Science in Applied Physics. Over the time period of 7 months, a fully operational automated probe- and laser annealing station has been constructed at the DiCarlo research group and integrated in the cleanroom environment of the Kavli Nanolab Institute. The setup has been developed with the vision of extended usage beyond the master project timeline.

During the project, successful laser annealing of Al/AlOx Josephson junctions has been demonstrated up to 12% resistance tuning with a resistance targeting accuracy of less than 0.4%. The accuracy and range limitations are discussed in detail, together with possible alterations to the setup to further enhance performance. The reliability of both junction characterization and thermal annealing suggests that this system can be used as part of the device fabrication cycle, namely a post-processing step for fine frequency targeting of superconducting transmon qubits. That said, additional research is advised to quantify the influence of thermal annealing on T_1 times.

The thesis is structured by stating a number of relevant concepts in the theory section (2) such as the transmon qubit, QuSurf architecture and active-feedback algorithm. This section is followed by an in depth discussion of the experimental setup (3), ranging from the optical components, laser safety considerations to operation software structure. Since testing and validation is a significant part of the project, the results section (4) mainly focuses on system performance. Besides performance metrics, this section discusses the very exciting laser annealing results as well as a first look into bi-directional annealing.

Research objectives:

- Reach sub-50 MHz targeting precision.
- Compare frequency and resistance measurements for individual surface-17 devices after fabrication (first resistance characterization), after cryogenic cooling and first frequency characterization, after warm-up and closed-loop annealing (second resistance characterization), after re-cooling to cryogenic temperatures and second frequency characterization.
- Develop closed-loop (active feedback) selective tuning of Josephson junctions using laser annealing.
- Construct laser safety enclosure, extend prior automated probe station (APS) setup to have the capabilities required for closed-loop annealing.
- Write and deploy control/interface software for APS system.

2 Theory

2.1 Flux Tunable Transmon

The most straightforward implementation of a superconducting circuit would be that of a dissipationless LC resonator. The Hamiltonian of this circuit corresponds to the quantum harmonic oscillator (QHO) which mimics a single particle in a one-dimensional quadratic potential and can be given in the charge-flux representation by:

$$\hat{H}_{QHO} = 4E_C\hat{n}^2 + \frac{1}{2}E_L\hat{\phi}^2, \tag{1}$$

where $E_C = e^2/(2C)$ is the charging energy which is required to add a single electron of charge e to an island of capacitance C. The inductive energy, given by $E_L = (\Phi_0/2\pi)^2/L$, is defined using the superconducting magnetic flux quantum $\Phi_0 = h/(2e)$. The operators $\hat{n} \equiv \hat{Q}/(2e)$ and $\hat{\phi} \equiv 2\pi\hat{\Phi}_{ext}/\Phi_0$ correspond to the charge and flux operators respectively. The eigenstates of this Hamiltonian are an infinite series of equally spaced levels E_k ($k \in \mathcal{W}$), where $E_{k+1} - E_k = \hbar\omega_r = \sqrt{8E_CE_L}$.

The flux-tunable transmon is a modification on the standard QHO. Addressing individual state transitions using a standard QHO is difficult due to the equidistant spacing of the energy levels. In order to comply with the second criterion of a functional quantum computer, it is essential to initiate a quantum system to any arbitrary state [7]. Therefore, anharmonicity is introduced by replacing the inductive component of the LC resonator by a non-linear element, namely a Josephson junction. This ensures that the transition frequencies are sufficiently distinguishable. To make this non-linear element flux tunable, a common approach is to use a superconducting quantum interference device (SQUID) [18]. For a flux tunable transmon with a SQUID loop and identical Josephson junctions, the circuit Hamiltonian is given by:

$$\hat{H}_{Transmon} = 4E_C\hat{n}^2 - 2E_J\,|\cos(\pi\Phi_{ext}/\Phi_0)|\cos(\hat{\phi}), \tag{2}$$

where $E_J = I_c\Phi_0/(2\pi)$ is the Josephson energy with I_c the critical current of the junction. The effect of external flux Φ_{ext} on the loop is further discussed in section 2.1.1. In the transmon limit, $E_J \gg E_C$, the energy potential of this Hamiltonian is essentially a weakly anharmonic oscillator [19, 20]. Taking the ground state $|0\rangle$ and first excited state $|1\rangle$ as computational subspace, the transition frequency can be approximated by $\omega_q = \omega_{01} \approx (\sqrt{8E_CE_J} - E_C)/\hbar$, also referred to as the qubit resonance frequency.

Figure 1 shows the schematic layout of a flux-tunable transmon circuit. Compared to the Cooper-pair box, the transmon is more resilient against charge noise (exponential suppression) [19, 21]. However, compared to a normal transmon, the flux-tunable transmon is consequentially sensitive to flux noise. This sensitivity can be reduced by making the two SQUID loop junctions asymmetrical at the cost of reducing the tunable frequency range [22, 23].

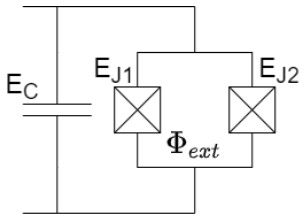

Figure 1: **Schematic of flux-tunable transmon**. Effective circuit diagram of the transmon qubit. The two Josephson junctions, forming the non-linear element with Josephson energies E_{J1} and E_{J2}, are shunted by a large capacitance with charging energy E_C. The current through the non-linear component is dependent on the external flux Φ_{ext}.

The transmon can be 'programmed' using a single qubit gate. Such a qubit gate operates on the computational subspace and is performed by applying microwave pulses at the transmon resonance frequency ω_q. The angle of rotation θ can be controlled by changing the amplitude of the pulse while the phase ϕ of the pulse corresponds to the phase of the rotation axis in the equatorial plane of the Bloch sphere [24, 25]. The matrix representation of an arbitrary rotation gate with the rotation axis in the xy-plane is given by:

$$R_{xy}(\phi,\theta) = \begin{bmatrix} \cos(\theta/2) & -ie^{-i\phi}\sin(\theta/2) \\ -ie^{i\phi}\sin(\theta/2) & \cos(\theta/2) \end{bmatrix}, \tag{3}$$

where θ and ϕ are continuous variables. When performing read-out on the qubit, the state information is projected onto the measurement basis (usually the computational basis). This process inherently losses information about the complete state. In the cQED architecture, read-out is performed by coupling a read-out resonator, with resonance frequency ω_r, to the qubit system. Both the resonator and qubit frequencies (ω_r and ω_q) are physically dependent on the material properties and design dimensions of the device. Ensuring a high accuracy in fabricating these designed resonance frequencies is paramount. Especially when scaling the number of transmons on a device, where multiplexing in the frequency domain is vital.

2.1.1 DC SQUID

The superconducting quantum interference device or SQUID is a flux sensitive device, based on a superconducting loop containing two parallel Josephson junctions. Figure 2 shows a schematic overview describing the SQUID loop as a component in the transmon circuit seen in figure 1. In the absence of an external magnetic field, the input current I_{tot} splits into the two branches with a ratio depending on the effective resistance ratio between both Josephson junctions. Assuming the junctions have an equal effective resistance, the input current is split equally resulting in $I_{tot}/2$ traversing each junction.

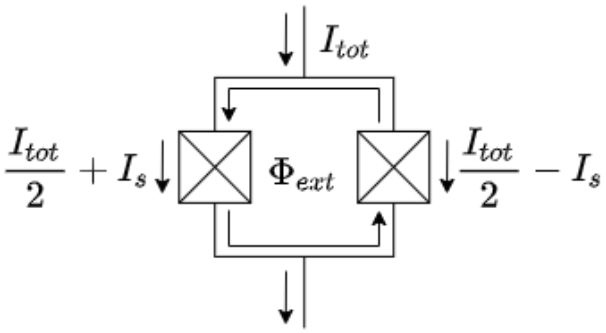

Figure 2: **Schematic of SQUID**. Two symmetric Josephson junctions in parallel forming a SQUID loop. With I_{tot} the total current going through the component, Φ_{ext} the flux generated by an external magnetic field and I_s the screening current induced by the flux.

Upon exposure to an external magnetic field, a screening current I_s, begins to circulate over the loop which ensures an integer number of flux quanta through the loop $n\Phi_0$ ($n \in \mathcal{Z}$). The direction of the screening current therefore depends on the external flux Φ_{ext} induced by the external magnetic field and in turn creates an additional Josephson phase ϕ. The screening current does not affect the total current, rather it re-distributes the current ratio over the two junctions by $I_{tot}/2 \pm I_s$ in either direction.

Once the current on either branch exceeds the critical current I_c, a non-zero voltage gradient emerges across the respective junction. This voltage is proportional to the time derivative of the difference in superconducting phase $\phi = \phi_1 - \phi_2 = 2\pi n + 2\pi\Phi_{ext}/\Phi_0$, ($n \in \mathcal{Z}$). Where $\phi_{1,2}$ describe the individual superconducting phase differences across the junctions 1 and 2 [18]. The critical current depends on the material properties of the superconductor, temperature and external magnetic field [26].

The external flux can be used as a control parameter. With the SQUID serving as the Josephson inductance in the transmon qubit, the Josephson energy E_J (and consequently, the qubit 0-1 transition frequency ω_{01}) can be tuned using an external magnetic field [19, 23, 27]. The tunability range is determined by the (a)symmetry of the Josephson energies E_{J1} and E_{J2}. The total flux-dependent Josephson energy E_J varies according to the following expression from [19]:

$$E_J(\Phi_{ext}) = E_{J\Sigma} \cos\left(\frac{\pi\Phi_{ext}}{\Phi_0}\right)\sqrt{1 + d^2 \tan\left(\frac{\pi\Phi_{ext}}{\Phi_0}\right)}, \tag{4}$$

where d is given as $d = (\alpha - 1)/(\alpha + 1)$, $\alpha = E_{J1}/E_{J2}$ is the ratio between Josephson energies and $E_{J\Sigma} = E_{J1} + E_{J2}$ is the sum of energies [23]. In the regime where $E_{J1} = E_{J2}$, the expression reduces to $E_J(\Phi_{ext}) = E_{J\Sigma} \cos(\pi\Phi_{ext}/\Phi_0)$.

2.1.2 Josephson Tunnel Junction

A Josephson junction consists of two weakly coupled superconducting electrodes separated by a thin insulating tunnel barrier of a thickness ranging between 1.5-2 nm. The insulating layer usually consists of an Al/AlOx/Al stack, where the oxide layer acts as the tunnel barrier. In the superconducting state, Cooper pairs tunnel through the barrier, inducing a supercurrent $I = I_c \sin(\phi)$, where I_c is the critical current and ϕ corresponds to the phase difference over the junction, between the order parameter in the two weakly coupled superconductors [26].

As mentioned in section 2.1.1, when the current across the junction exceeds the critical current, the proportionality between the voltage (V) across the junction and the time derivative of the difference in superconducting phase can be given as:

$$\frac{\partial \phi}{\partial t} = \frac{2\pi}{\Phi_0} V, \tag{5}$$

This allows for the phase-dependent Josephson inductance $L(\phi)$ to be derived using the time derivative of the induced supercurrent over the junction ($\frac{\partial I}{\partial \phi} = I_c \cos(\phi)$) and Faraday's law ($V = L(\phi)\frac{\partial I}{\partial t}$) [28]:

$$\begin{aligned} \frac{\partial I}{\partial t} &= \frac{\partial I}{\partial \phi}\frac{\partial \phi}{\partial t} = I_c \cos(\phi)\frac{2\pi}{\Phi_0} V, \\ L(\phi) &= \frac{\Phi_0}{2\pi I_c \cos(\phi)} = \frac{L_J}{\cos(\phi)}, \end{aligned} \tag{6}$$

where $L_J = L(0) = \Phi_0/(2\pi I_c)$. Note that the non-linear behaviour of the Josephson inductance comes from the $\cos(\phi)$ dependence. The junction resistance depends on the thickness and surface area of the insulating layer. It is known that junctions are prone to (anti-)aging which corresponds to increasing or decreasing of tunnel barrier resistance over time. The mechanism behind this process not completely understood. The process of thermal annealing discussed in this thesis aims to provide a better insight into the conditions required for (anti-)aging.

2.2 QuSurf Architecture

The QuSurf program is jointly developed by TU Delft, TNO, ETH Zürich and Zurich Instruments under the IARPA LogiQ project division. The program aims to realize a fault tolerant logical quantum bit, based on a superconducting circuit implementation of the surface code architecture [8, 9, 29, 30]. The idea behind the QuSurf architecture is to have a scalable approach to toggling nearest neighbor qubit control while maintaining sufficient individual coherence times to perform single and two-qubit gates. In contrary to other literature which might utilize fixed-frequencey qubits, cross resonance gates [16] or fixed-frequency qubits, tunable couplers [6], this architecture specifically focusses on tunable-frequency qubits instead [31–33].

The 'only' nearest-neighbor qubit interaction model is realized using the surface code paradigm, designed for fault-tolerant quantum computing. The surface code defines a unit cell in the quantum plane that can be repeated to increase system capability without increasing the complexity of the unit cell. For example, a unit cell should enable quantum interconnect between cells for seamless nearest-neighbor interactions, all qubits within the cell should be independently addressable and the unit cell should contain suitable classical interconnect to and from the control plane [9]. In theory, after solving the unit cell, one can scale up indefinitely[2]. The QuSurf architecture proposes a scalable scheme for the quantum error correction cycle of a monolithic superconducting surface code by defining a unit cell that satisfies these requirements.

Figure 3a shows the surface-code fabric by repetition of eight-qubit unit cells. The cell contains four data qubits (D_1 to D_4) and four ancillas qubits (X_1, X_2, Z_1 and Z_2). The importance of the ancilla qubits can not be understated and is essential for performing stabilizer measurements and the error correction protocols. This thesis however, will not focus on the wonderful world of error correction. Instead, the arrangement of data- and ancilla qubits within the unit cell is especially interesting when focusing on the spatial- and frequency multiplexing required for such a surface-code. Most notably, the different qubit frequency groups.

To introduce the frequency groups, it helps to first consider the two qubit CZ or controlled-Z gate which is commonly used to map the parity of multiple data qubits onto ancilla qubits during the X or Z stabilizer measurements. The CZ gate utilizes the avoided crossing between the $|11\rangle$ and $|02\rangle$ state of

[2] This statement is far from trivial however, as there are known bottlenecks when scaling up beyond the unit cell such as frequency targeting, coherence times and temperature control.

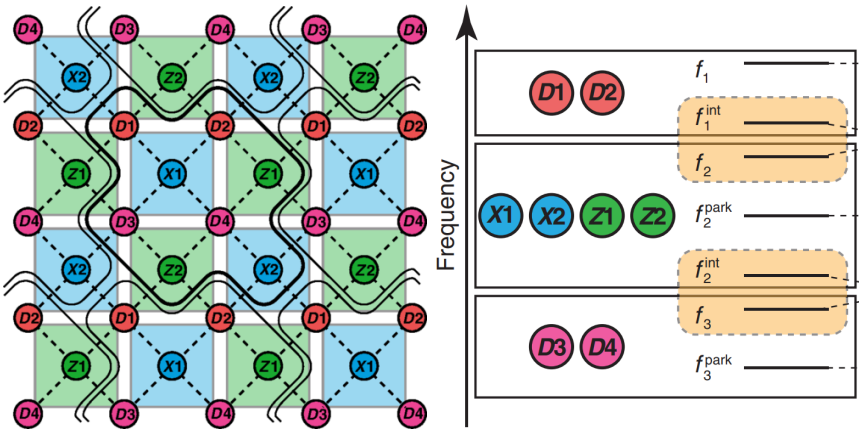

(a) (b)

Figure 3: **Surface-code Unit cell**. A repeated surface-code fabric using 8-qubit unit cells (a). The circles labeled 'D' represent data-qubits while the circles labeled 'Z' and 'X' represent ancilla-qubits. The green and blue plaquettes define the X- and Z-type stabilizer measurement connections respectively. (b) A schematic showing the distribution of data- and ancilla-qubits within the three frequency groups. (Source: [9])

two coupled transmons. By design, both qubit resonance-sweetspot frequencies are sufficiently far apart such that interaction is minimal. To implement a CZ gate, the qubit at the higher frequency is slowly detuned to the interaction zone[3] and back after experiencing a frequency shift conditioned on the lower frequency qubit state (see figure 3b). In a planar configuration with only nearest neighbor interactions, two frequency groups would be sufficient to prevent idle-state interactions. However, any operation that involves qubit interaction by closing the frequency gap requires all neighboring qubits that exist near these operating frequencies to be temporarily 'parked' at a different frequency. For any two-qubit gate, this introduces an overhead in operations that need to be performed. Defining additional idle-frequency groups reduces this overhead but creates the problem of frequency collision (isolation).

In an attempt to balance the two, the QuSurf architecture defines 3 frequency groups[4]: Low, Medium and High at 4.9, 6.0 and 6.7 GHz respectively. In the case of the 8-qubit unit cell, D_1 and D_2 are part of the high-frequency group, D_3 and D_4 part of the low-frequency group and all ancilla qubits are part of the mid-frequency group. Due to the heavy reliance on frequency modulation in reducing idle interactions and performing reliable error correction protocols, the frequency targeting of individual qubits is very important.

2.2.1 Qubit Frequency Targeting

From section 2.1 the qubit transition frequency from the ground state $|0\rangle$ to the first excited state $|1\rangle$ is given by an approximation in the form of $\omega_{01} \approx (\sqrt{8E_C E_J} - E_C)/\hbar$. This provides a relation between the Josephson energy, charging energy and the transition frequency for a transmon circuit. In the transmon limit ($E_J \gg E_C$), this facilitates a control parameter based on the critical current. Unfortunately, talking about the critical current is only relevant at cryogenic temperatures and is not something which is easily measured after fabrication. Instead, the room-temperature (normal-state) junction resistance is used as a control parameter for the Josephson energy. In theory this relation is established using the Ambegaokar-Baratoff formula [34] and transmon theory [19], which couple the critical current and normal-state resistance to the Josephson energy using the superconducting gap energy. In practice however, this ratio between the Josephson energy and normal-state resistance is experimentally calibrated and expessed as follows:

$$E_J = \frac{M}{R_n}, \tag{7}$$

[3] The interaction zone is defined where two qubit frequencies are sufficiently close to influence each other.
[4] Besides the qubits, the readout-purcell resonator pairs are placed above the high-frequency group at a range 7-8 GHz.

where M is the experimentally calibrated factor and R_n the normal-state resistance. This resistance refers to the total resistance of the non-linear inductive component of the transmon circuit. In the case of a flux-tunable transmon, this refers to the SQUID loop with a pair of two parallel Josephson junctions. Assuming the transmon limit, the transition frequency relation can be related to the normal-state resistance by:

$$\omega_{01} \approx \frac{M^*}{\sqrt{R_n}}, \tag{8}$$

where $M^* = \sqrt{8E_C M}/\hbar$. Relevant for quantifying the accuracy of predicting the transition frequency using the normal-state resistance, is the one-over-square-root relation. This also implies that the tunability range in percentage for the resistance is double compared to frequency. Frequency targeting is the process of designing, fabricating and tuning Josephson junction resistances in order to achieve the desired transition frequency of a transmon qubit at cryogenic temperatures. When the qubit frequency is not on target, this can result in unwanted interactions between qubits.

2.2.2 Residual ZZ-Coupling

The QuSurf architecture hosts two main forms of idle crosstalk. These are residual interactions between nearest-neighbor qubits and residual exchange interactions between next-nearest-neighbor qubits with the same frequency. Both class of interacitons violate locatilty [12]. In quantum electrodynamics, crosstalk usually refers to unwanted terms in the Hamiltonian [13, 35]. This is particularly relevant in superconducting qubit architecture which require a high degree of control over nearest neighbor interactions in the form of single- and two-qubit gate errors [11, 36–38].

In systems where multiple transmon qubits are coupled via bus resonators, the coupling between their higher energy-levels give rise to cross-Kerr interactions that can be described by $\zeta_{ij} a_i^\dagger a_i a_j^\dagger a_j$ [31], where ζ_{ij} corresponds to the frequency shift of the qubit state i depending on qubit state j and vice versa. This type of idle ZZ-crosstalk causes dephasing in the qubits if ζ_{ij} is comparable to the qubit decoherence rate. For an idle time τ, the coherent correlated ZZ error can be expressed as a rotation angle:

$$\theta(\tau) = \frac{\zeta_{ij}\tau}{4}. \tag{9}$$

This error source depends strongly on the idle frequency of the qubits and thus strongly on deviations in qubit frequency targeting. Using perturbation theory for a typical CZ operation the frequency shift $\zeta_{ij} = \hbar\omega_{11} - \hbar\omega_{01} - \hbar\omega_{10}$ can be approximated by [39]:

$$\zeta_{ij} = \frac{J_2^2}{\hbar}\left(\frac{1}{\omega_{20} - \omega_{11}} + \frac{1}{\omega_{02} - \omega_{11}}\right), \tag{10}$$

where J_2 is the effective coupling strength between qubits i and j and the angular frequency (ω_{pq}) subscripts represent the number of excitations in qubit levels i and j respectively. The residual ZZ-coupling can be measured from the frequency difference $\Delta\omega_i^{(j)}$ of Ramsey oscillations on neighboring qubits i and j in state $|1\rangle$ and $|0\rangle$. This frequency difference measurement can be implemented using an echo experiment described in [39, figure A.2].

2.3 Laser Optics

With all the interesting and sophisticated setups one can create using laser optics, this section will mainly focus on some rudimentary subjects related to performing controlled thermal annealing using a single laser source. This experimentalist approach works under the assumption of the geometrical optical limit, which is applicable given the criteria of this problem [40]. The optical setup schematic can be found in section 3.1. This setup focuses a multimode laser beam with known frequency λ, diameter D_0 and divergence Θ through an objective lens onto a sample. The objective is to determine the minimum achievable beam spot on the sample given the limited optical components.

2.3.1 Beam Width

To prevent confusion, the 'beam width' is defined as the diameter of the laser beam, up to the point where the intensity decreases to $1/e^2$ of the maximum intensity. The beam waist (or beam focus) is the location along the propagation direction where the beam width has a minimum.

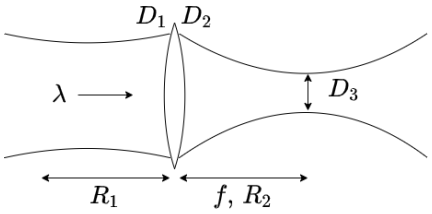

Figure 4: **Schematic Estimation of Beam Shape**. Relevant parameters regarding the focused beam by the objective lens. D_1 and D_2 are the beam widths before and after the objective lens respectively. D_3 is the beam waist at the sample-side. λ is the source wavelength, f the focal length of the objective lens and R_2 the radius of curvature of the light on the sample-side.

Calculating the theoretical beam width and distance from the lens based on [41]. Approximations done in geometric optic limit. For a more accurate calculation of the distance z_2 between the beam waist and the lens, the divergence of the laser source should be taken into account with finite R_1. Instead, the assumption is made for $R_2 = [1/f - 1/R_1]^{-1} \approx f$. The M^2 factor, also known as beam quality factor, is commonly used to define the beam quality. This factor is related to the half-angle beam divergence $\Theta = M^2\lambda/\pi D_0$, where D_0 is the default beam waist of the laser. A diffraction-limited (Gaussian) beam has an M^2 factor of 1 and acts as a lower limit [42]. Because the considered laser source has multiple transverse modes with unknown M^2 factor, the following relations will become lower limits instead. Using these assumptions, an estimation is made for the beam waist and its distance from the objective lens:

$$z_2 = \frac{R_2}{1 + \left(\frac{4M^2 R_2}{\pi D_2^2/\lambda}\right)^2}, \text{ for } R_2 << \frac{\pi D_2^2}{4\lambda M^2} \rightarrow z_2 \approx R_2 \tag{11}$$

$$D_3 = \frac{D_2}{\sqrt{1 + \left(\frac{\pi D_2^2/\lambda}{4M^2 R_2}\right)^2}}, \text{ for } R_2 << \frac{\pi D_2^2}{4\lambda M^2} \rightarrow D_3 \geq \frac{4\lambda R_2}{\pi D_2} \tag{12}$$

For the current setup, laser source $\lambda \approx 405$ nm, outgoing radius of curvature $R_2 \approx -f = 200$ mm and the beam width post lens $D_2 = 2.3$ mm. By convention, the radius of curvature is defined as negative when the center is to the right. This results in a minimal beam width of roughly 45 μm.

2.3.2 Power and Energy Density

Knowing the lower-limit beam spot diameter ($d = D_3$) on the sample, the initial laser source power (P), the exposure time (τ) and the losses introduced by optical components (including medium) (η) allows

for the calculation of the power and energy surface-density:

$$\begin{aligned} P_{density} =& \frac{(1-\eta)P}{\pi d^2/4} \left[\frac{W}{m^2}\right] \\ E_{density} =& P_{density}\tau \left[\frac{J}{m^2}\right] \end{aligned} \tag{13}$$

For the current setup, the laser power can theoretically be set up to $P \approx 10^3\ mW$. The losses introduced by the optical components are studied extensively in section 3.1.1 and 3.1.2, with a measured loss factor of $\eta = 0.45$ (predicted: $\eta = 0.35$). A generous estimation of the beam-spot diameter would be $d \approx 5 \cdot 10^1 \mu m$. This results in a predicted power density of $P_{density} \approx 0.28 \cdot 10^9\ W/m^2$. Note that since the laser hosts more than just TEM_{00}, the power density distribution is not necessarily described by a Gaussian wavefront.

2.4 Active Feedback Algorithm

The algorithm behind the active feedback control described in section 3.5 evaluates junction-pair resistance measurements and predicts their tuning behaviour under thermal annealing based on these data points. Each junction-pair is evaluated individually. The tuning behaviour is described by a series of resistance measurements $r(t)$, where t is the total thermal annealing exposure time experienced by the junction-pair. The current version of the algorithm assumes a set laser-power output throughout the experiment and a mono-directional annealing response. As a consequence, time is the only control parameter during the active feedback protocol. Each junction-pair starts with at least one initial measurement value $r_0 = r(0)$. The tuning behaviour is normalized based on this starting value:

$$y(t) = \frac{r(t) - r_0}{r_0}, \tag{14}$$

where $y(t)$ is the normalized change in resistance depending on total exposure time t. One of the advantages of this algorithm is the ability to define a unique target resistance r_T for each junction-pair. The corresponding normalized target is defined as $y_T = (r_T - r_0)/r_0$. The algorithm defines the following 3 completion criteria:

1. $y_T \leq 0$, "Target equal or bellow starting value."
2. $y(t) \geq y_T$, "Current value equal or above target."
3. $t \geq t_{max}$, "Maximum exposure time reached."

where t_{max} is an arbitrary upper limit for the maximum exposure time (experiment time). If either one of these three criteria is triggered for any junction-pair, that junction-pair no longer receives annealing. When all junction-pairs satisfy one of the completion criteria the algorithm is finished.

In order to predict the exposure time required to tune a junction-pair from their starting resistance to the target resistance, an initial guess or ansatz is required. Based on empirical measurements, the fit-function, used as ansatz, is defined as a power-law distribution:

$$f_{\alpha,\delta}(t) : t \to \alpha t^{1/\delta}, \tag{15}$$

where α and δ are fit parameters which are strongly correlated to the thermal annealing power (see figure 15). In the trivial case the junction-pair starts out un-exposed where $y_0 = y(t_0) = 0$ and is tuned until $y(t) = y_T - y_0 = y_T$. The total exposure time Δt_{0T} is calculated based on the inverse of the fit-function:

$$\begin{aligned} g_{\alpha,\delta}(y) : y \to& \left[\frac{1}{\alpha} y\right]^{\delta} \\ \Delta t_{0T} = t_T - t_0 =& g_{\alpha,\delta}\left(y_T - y_0\right) = g_{\alpha,\delta}\left(y_T\right), \end{aligned} \tag{16}$$

where $g_{\alpha,\delta}$ is the inverse fit-function and Δt_{0T} is the exact exposure time required to tune a junction-pair from r_0 to r_T (target resistance). To decrease the reliability on fixed parameters such as α and δ which may need to vary from junction to junction depending on slight deviations in their barrier thickness[5], an iterative parameterization is introduced. The new parameters α_i and δ_i are optimized based on the original fit-function and prior measurement set $y_i \in Y$ (where $i \in \{0, 1, ..., T\}$):

[5] It is expected that junctions with different tunnel barrier thickness respond slightly different to thermal annealing.

$$\min_{\alpha_i,\delta_i} \quad \sqrt{\frac{1}{i}\sum_{j=0}^{i-1}\left(y(t_j) - f_{\alpha_i,\delta_i}(t_j)\right)^2}, \qquad i > 0, \tag{17}$$

where $y(t_j)$ is y_j measured after Δt_{0j} exposure time. Note the boundary condition for $i = 0$ where $\alpha_0 = \alpha$ and $\delta_0 = \delta$, equal to the ansatz parameters respectively. Also note that root-mean-square optimizer is arbitrary, any optimizer that fits f_{α_i,δ_i} to the data set Y should be sufficient. This optimization step essentially ensures that the algorithm 'learns' the tuning behaviour for individual junction-pairs which significantly improves the targeting accuracy as well as reducing dependency on the initial guess.

In practice, the trivial case where none of the junction-pairs have experiences thermal exposure is not necessarily correct. For example, prior exposure can occur from prior annealing experiments, air-bridge annealing or natural aging. Whatever the case, the algorithm is able to handle these perturbations by assuming the experiment to starts at y_1 (r_1), where r_0 and Δt_{01} are unknowns. Due to the percentage tuning convention, it is possible to take $y_0 = 0$ without loss of generality. Since y_1 is measurable and y_T is known, the remaining exposure time Δt_{1T} can be derived from the following relations:

$$\begin{aligned} \Delta t_{01} &= g_{\alpha_i,\delta_i}(y_1 - y_0) = g_{\alpha_i,\delta_i}(y_1) \\ \Delta t_{01} + \Delta t_{1T} &= g_{\alpha_i,\delta_i}(y_T - y_0) = g_{\alpha_i,\delta_i}(y_T) \\ \Delta t_{1T} &= g_{\alpha_i,\delta_i}(y_T) - g_{\alpha_i,\delta_i}(y_1), \end{aligned} \tag{18}$$

where Δt_{1T} can be numerically approximated. Lastly, there are two precautions built in the algorithm to prevent 'overshooting' the target resistance. This is especially important for as long as there is no solution to bi-directional annealing. The first precaution focuses on the exposure time Δt_{iT}. Instead of exposing the full duration, the exposure time is multiplied by a fraction m with $0 < m \leq 1$:

$$\begin{aligned} &\Delta t_{i(i+1)} = m \cdot \Delta t_{iT}, \\ &\text{where } m = 1 \text{ if } \Delta t_{iT} \leq \Delta t_{min}, \text{ else } m \neq 0, \end{aligned} \tag{19}$$

where Δt_{iT} is the predicted total exposure time required (from y_i to y_T), $\Delta t_{i(i+1)}$ is the fractional exposure time applied (from y_i to y_{i+1}) and Δt_{min} is a minimum exposure time threshold to prevent asymptotic tuning. The second precaution is performed in combination with the basic automated probe station (APS) functionality, which includes averaging over multiple resistance measurement in a single round i in between thermal annealing exposure. In other words, y_i is averaged over multiple resistance measurements:

$$y(t) = \frac{\frac{1}{N}\sum_{k=0}^{N-1} r(t)^k - r_0}{r_0}, \tag{20}$$

where N is a non-zero integer (by default $N = 3$). This precaution handles measurement anomalies.

3 Experimental Setup

This project setup builds on earlier work conducted by members of the research group. In their effort to scale up device fabrication to wafer scale, an early prototype was build that automatically characterizes Josephson junction conductances with a 2-point measurement setup. This prototype has seen continues development throughout the project. Under which an extension to the measurement functionality by utilizing a 4-point setup for improved reliability, as well as the addition of a fully automated laser annealing stack. The experimental setup design can be separated in three distinct sections:

- **Laser optics**. Responsible for focusing a non-pulse laser on a specific device location, while controlling its exposure time, wavelength and optical feedback. This includes the laser, alignment mirrors, beam-shutter, diochric mirror, objective lens and CCD-camera .
- **Laser safety enclosure**. Because of the high power class-4 laser, a professional laser enclosure is required, especially when operated in a cleanroom environment. This includes a completely opaque and laser-proof enclosure, opening hatch with magnetic interlock and a safety overwrite switch connected to the laser power supply (PSU).
- **Probing mechanism**. Responsible for controlling the movement for the quantum device and landing the probe to perform conductance measurements. This includes the motorized stages, the probe needles and the measurement electronics behind it.

Besides the hardware components, the setup is also fully controllable through a digital interface. This allows for automated probing and laser annealing. A significant amount of effort has been put into designing a scalable back-end system that can process devices regardless of their design details.

3.1 Optical Setup

The optical setup is schematically shown in figure 5. A beam shutter controls the exposure time of a violet diode laser at wavelength $\lambda = 405$ nm, producing a beam of 2.3 mm in diameter. The beam passes through an optional beamsplitter into a set of protected aluminium mirrors. These mirrors can be manually adjusted to align the beam with the dichroic mirror and reflected through the objective lens, onto the sample device. The beamsplitter is optional since the setup does not necessarily require feedback information on the power-output, however this will be important for quantifying the output power variation during laser annealing in future iterations.

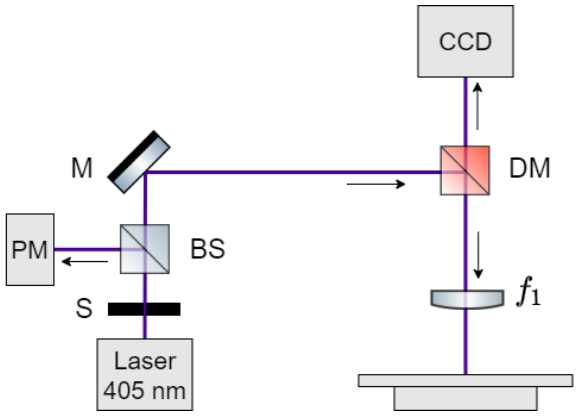

Figure 5: **Schematic Representation of the Optical Setup**. Including: beam shutter (S), optional beamsplitter (BS), optional power output sensor (PM), long-pass dichroic mirror (DM), infinity-corrected objective lens (f_1) and a DCx uc480 CCD-camera .

The dichroic mirror acts as a long-pass filter with a cutoff wavelength at 425 nm and a reflection band at $380 - 410$ nm. Light reflected from the sample above this cutoff wavelength have a chance of passing through the objective lens and dichroic mirror to arrive at the CCD-camera . This allows the view of both the device and the beamspot through a 10-times magnification lens. The live feedback is essential during device alignment. The laser source wavelength is chosen to optimize absorption by Al/AlOx that makes up the junctions, while minimizing absorption with the silicon substrate. The objective lens, dichroic

mirror and the CCD-camera are physically connected to form the vertical-optics stage. This stage is mounted to a support structure (not visible in the schematic) and can be re-positioned in along the x, y or z-axis. Additionally, the dichroic mirror together with the objective lens can rotate along the optical axis (seen vertical in figure 5). The objective lens has two tasks, the first is to produce an enlarged image of the sample which is processed by the camera, the second is to focus the laser beam onto the sample.

Note that the difference in focal length between the visual spectrum and the beam wavelength is neglected. This results in the laser being slightly out of focus on the sample, as the objective length is determined based on a focused image in the visual spectrum. For details, see section 2.3.1. It is also assumed that the incident beam, entering the objective lens, is collimated and parallel to the optical-axis. Both of these assumptions are sufficient with the current objective of uniformly annealing both junctions within the squid-loop. Based on a Gaussian wavefront, the radial power-density gradient scales inversely with the spot-size. This implies an increased uniformity in power density at the center of the beamspot.

In future iterations, where it becomes interesting to perform asymmetric annealing of junction-pairs to reduce sensitivity to flux noise, the beamspot size requirement will become more stringent. A possible approach would be to place a collimating- and concave lens duo in front of the dichroic mirror. The collimating lens will assure the beam source to be focused at infinity, while the concave lens acts as a focal point correcting lens for the low-wavelength beam before entering the main objective lens.

3.1.1 Components

In order to correctly route the beam path to the dichroic mirror while considering its vertical degree of freedom, the set of mirrors shown in figure 5 are part of a periscope setup. The periscope creates the necessary additional degrees of freedom required when working with a stationary laser source and a relatively flexible vertical-optics stage. The periscope uses two protected aluminum mirrors that adjust the beam path at an approximate 45° angle of incidence (AOI).

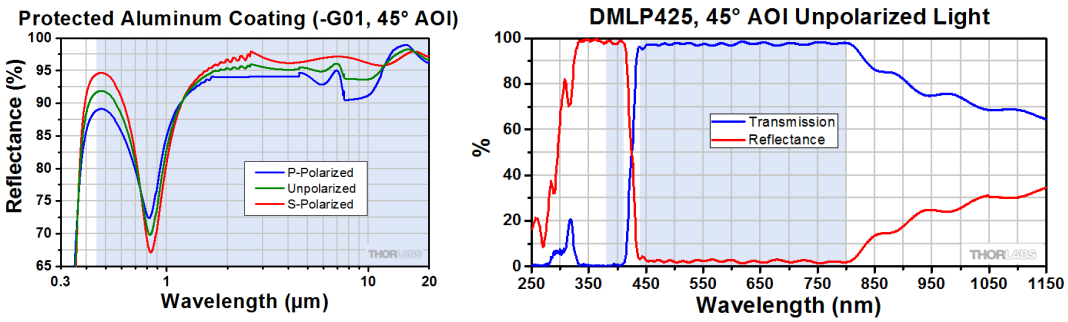

(a) (b)

Figure 6: **Mirror Reflectance**. Tested reflectivity graph for the protected aluminum periscope mirrors (a) and long-pass dichrioc mirror (B) at various wavelengths (Source: Thorlabs).

Figure 6a and 6b show the reflectance of the periscope mirrors and dichroic mirror respectively. At the operating wavelength of 405nm, the predicted average reflectance of the periscope mirrors is 87.5%, assuming 45° AOI and an equal distribution of P- and S-polarziation[6]. The Dichroic mirror has an average reflectance of $> 95\%$, assuming 45° AOI. Unfortunately, the transmission spectrum of the objective lens is not publicly shared by the manufacturer[7]. Instead, the typical transmission spectrum can be derived from similar long-distance, infinity corrected objective lenses on the market. To predict the total loss over the optics, an average transmission of 85% will be used for the objective lens and a generous 100% reflectance for the dichroic mirror (at the 405 nm wavelength). The predicted total loss is then given by:

$$\eta_{predict} = (1 - R^2_{mirror} \times R_{dichroic} \times T_{lens}), \tag{21}$$

where R_{mirror} and $R_{dichroic}$ are the periscope mirror and dichroic mirror reflectance coefficient respectively and T_{lens} is the objective lens transmission coefficient. This gives a lower bound loss coefficient of $\eta_{predict} \approx 35\%$.

[6]The periscope is arranged in such a configuration that the beam path makes an 45° angle in the horizontal plane, creating an (almost) equal distribution of P- and S-polarized reflections.

[7]Edmund optics does not publicly share the transmission spectra on their website.

3.1.2 Power Output

The laser power is characterized for different PSU currents both in front of the beam shutter and after the objective lens, which will be refered to as pre- and post-optics respectively. The considered PSU current ranges between 50 and 800 mA, with a region of interest near the activation threshold (303 mA) between 290 and 510 mA.

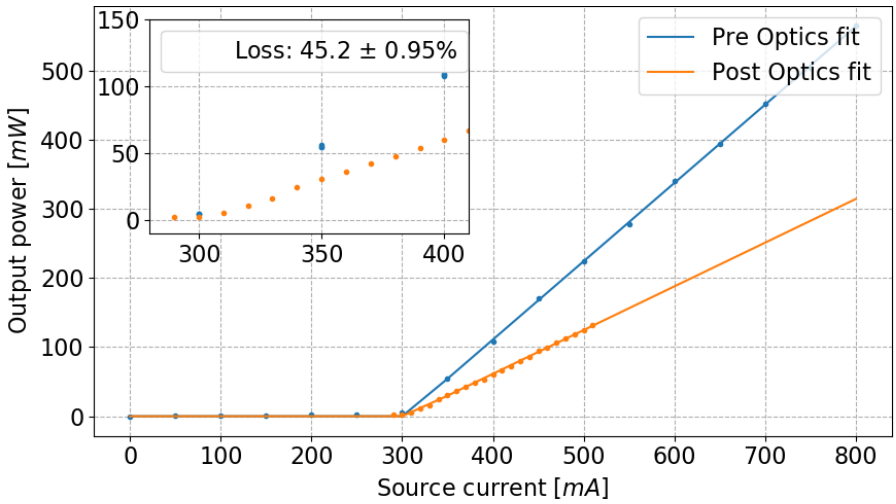

Figure 7: **Laser Power Sweep**. An experimental characterization of the effective laser power both in front of the beam shutter (pre-optics) and after the objective lens (post-optics). The observed activation threshold is at 303 mA. The calculated respective slopes are 1.312 and 0.632 mW/mA. Indicating a loss factor of 45.2% ± 0.95%.

A ReLu-fit function is used to determine the activation threshold and slope of the relation between PSU current and output power (assuming a linear relation). The respective slopes are used to determine the loss factor due to scattering, absorption and transmission through the optics. The apparent additional loss of 10% with respect to the lower bound calculation of previous section can be contributed to an imperfect reflectance coefficient of the dichroic mirror, the interaction with the medium or the non-zero divergence term in the laser source.

3.1.3 Laser Alignment

This section is intended as a guide for aligning the laser setup. Figure 8 provides a schematic overview of the main optical components used to achieve alignment. The following strategy can be used to align the setup from scratch:

1. Translate the vertical-optics stage such that the sample is in focus and the probe needles are in field of view[8]. Use the CCD-camera to verify this step.

2. Asses the intensity throughout the beam path and apply appropriate neutral density (ND) filters accordingly. The current setup hosts two intensity levels, before and after the focusing objective lens.

3. Place a temporary optical cover over the laser source and ND filter to eliminate stray light. Place power meter directly after the ND filter. Ensure all participants wear certified laser-protection glasses before continuing.

4. Turn the laser on and verify if the ND filter has the desired effect of reducing the laser intensity to a 'safe' value[9]. If not, turn off the laser and repeat step 2-4.

5. Remove the power meter and verify a visible spot with alignment paper.

[8] Note, the probe needles are only visible when they are within 0.5 mm from the sample due to the long-working lens focus length.

[9] Defined by the international guidelines on laser safety.

6. Translate the periscope to intersect the beam path with the lower mirror. Rotate the lower mirror to route the beam path up to the center of the upper periscope mirror. Translate the upper mirror in height to match the dichroic mirror of the vertical-optics stage. Rotate the upper mirror to route the beam path into the dichroic mirror cube.

7. Rotate the vertical-optics stage until the beamspot is visible as a reflection off the sample into the CCD-camera . Ensure the beam path hits the dichroic mirror at the center and not the edge to reduce unwanted deformation of the beamspot. For fine adjustments in beamspot position and shape, use the pitch and yaw rotations on the upper and lower periscope mirrors.

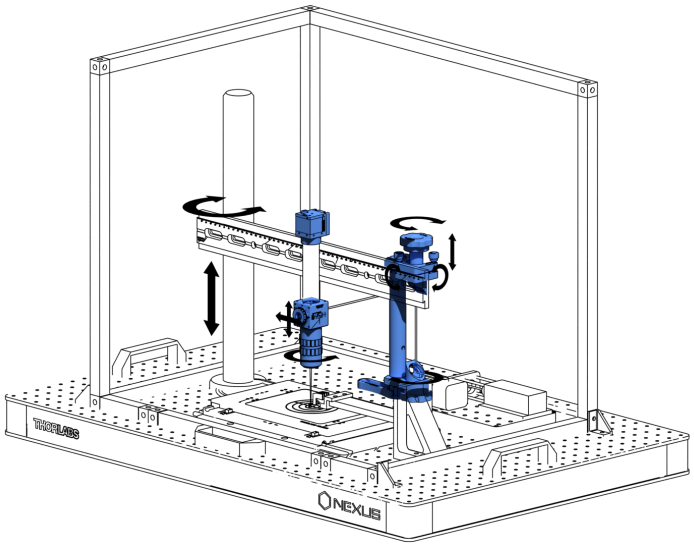

Figure 8: **Laser Alignment Axis**. Line schematic of the experimental setup. For improved visibility, part of the enclosure is hidden. The optical components including: CCD-camera , periscope, dichroic mirror cube and objective lens are highlighted in color. Black arrows indicate the respective degrees of freedom for each component.

3.2 Laser Safety

The laser that will be used for annealing is a high stability diode laser which is designed to operate at 405 ± 5 nm wavelength. The power output can be manually or digitally controlled, ranging from $<$1 to 1000 mW. This makes it a class-4 laser. For any laser-utilising system operating in a cleanroom environment it is required to reduce the setup to a class-1 system. By definition, class-1 systems are safe under all conditions of normal use. This is achieved by utilizing a range of safety procedures, such as installing a laser-safety enclosure around the setup to contain stray radiation resulting from diffuse surface reflections. An interlock switch is installed and connected to the power supply which creates a closed circuit that is interrupted when the enclosure is opened up. Upon triggering the interlock and breaking the circuit, the laser switches to an alarm mode, meaning it shuts off and requires both the interlock circuit to be closed as well as a manual reset using the key switch before resuming operations.

The laser diode has no active cooling as it relies on passive heat diffusion either to the surrounding atmosphere or the metal breadboard to which it is mounted. As a precaution, the software is designed to keep track of the laser operation time and enforces regular intervals in which the annealing process is paused and the laser is turned off. The cooldown time depends on the power at which the laser is operating and is estimated empirically based on monitored test runs.

3.2.1 Enclosure

The optical enclosure is a custom design specifically developed for this project. It provides a protected space that removes the risk of high-intensity laser exposure. The enclosure, schematically visualized in figure 9b, consists of two frames connected to an optical breadboard. The frames are separated into a main frame and a hatch frame. Both frames are constructed using 25mm construction rails, slotted-corner cubes and 6mm low-profile screws. They are connected using 2 hinges connected on the top of

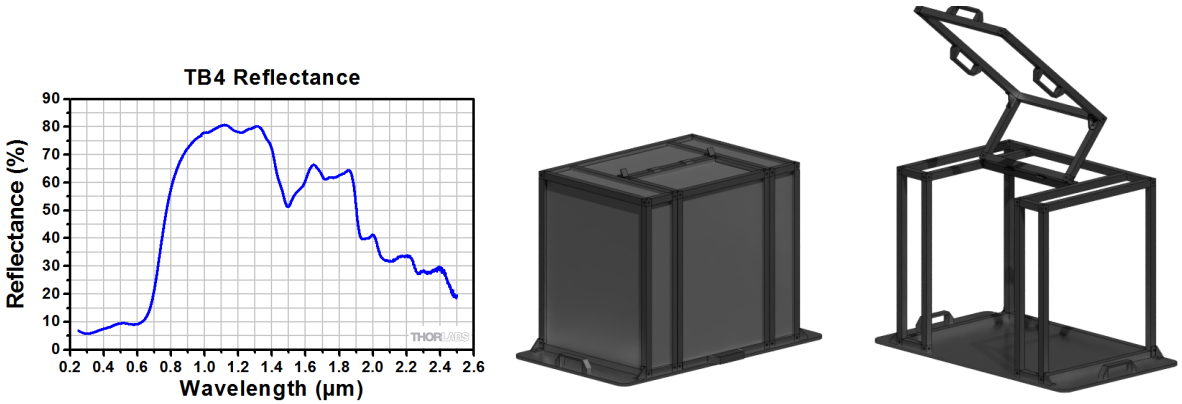

(a) (b)

Figure 9: **Laser Safety Enclosure**. Tested reflectivity graph (a) for the hardboard enclosure panels at various wavelengths (Source: Thorlabs). The operational wavelength of 405nm (0.4μm) corresponds to a reflectance of roughly 8%. (b) A rendered view of the custom-designed safety enclosure with and without outer panels. The enclosure dimensions are: 750mm width, 550mm depth, 550mm height (excluding the breadboard).

the enclosure. The dimensions are chosen such that most of the construction rails can be off-the-shelve ordered to reduce lead-times, while ensuring enough internal space for the necessary components and potential future upgrades. Another constraint while designing the enclosure was the limited available operation space within the cleanroom.

The outer panels consist of 4.76mm thick, black hardboard with a foam-core. These panels are designed to control stray or ambient light. Figure 9a shows the tested reflectivity of these panels, performed by the manufacturer. This data is obtained at 8° angle of incidence (AOI). At the laser source operational wavelength of 405nm (0.4μm), the reflectivity corresponds to roughly 8%. Inside the enclosure there are aluminium panels strategically placed to limit internal reflections.

In order to allow cable management in and out of the enclosure while maintaining the laser-safety integrity, an umbilical design is implemented. One of the side panels is modified to have a small opening, covered with packaging foam from the inside. This creates a single point of entry for electronics, vacuum line and interlock connection. The opening on the inside is shielded from the stray laser-light using an aluminium panel. The cables exit the enclosure under an angle to reduce light 'leakage'.

In future iterations the umbilical design might be replaced with a dedicated interface panel. Where all communication in and out of the enclosure can be passed through vacuum, BNC, USB and RS232 mounting ports. This reduces maintenance and increases safety and reliability.

3.2.2 Interlock

The interlock system is meant as a safety feature to effectively reduce the overall system with a class-4 laser, down to a class-1 system under normal operation conditions. Where 'normal operation conditions' refers to device characterization and laser annealing. This excludes general maintenance and/or laser alignment which should only be performed by certified personnel. Figure 10 shows an interaction flowchart with respect to the laser source. The laser power supply unit (PSU) is activated or de-activated using a standard key-lock mechanism. The interlock system is based on an additional overhead circuit that needs to be uninterrupted for the laser to function. This circuit is dependent on both the magnetic interlock connected to the enclosure hatch and a kill switch. If the interlock circuit is interrupted in any way, the PSU goes into 'alarm' mode, during which the laser is immediately shutdown. Only a manual reset can recover the PSU from this state. The magnetic switch is mounted to both the main-frame and hatch-frame, creating the closed loop circuit if and only if the hatch is fully closed. The effective contact width of the sensor is 1cm. This means the interlock circuit will be broken well before the hatch is fully separated from the main body (due to the 2.5cm thickness of the hatch frame). None of the optical components are motorized, resulting in a static beam path. This ensures that the enclosure will only receive diffused light, either from imperfections in the optical components, the closed beam shutter, the bare XY-stage or the sample.

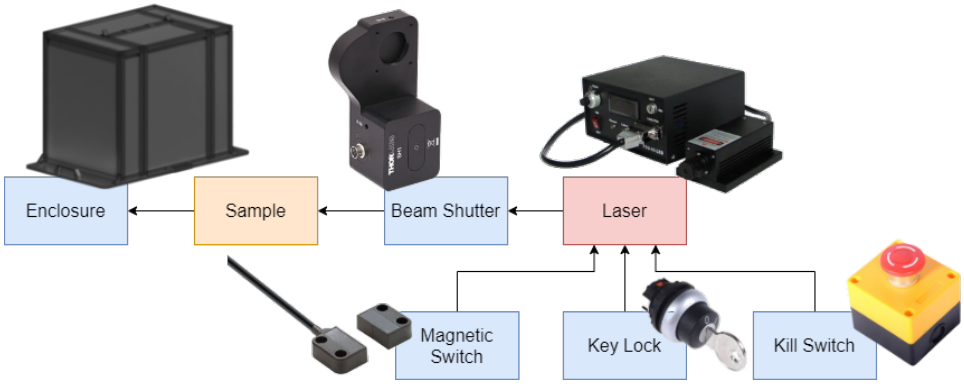

Figure 10: **Interlock System Diagram**. The interlock system consists of a standard key-lock integrated in the laser PSU, a magnetic switch connected to the enclosure frame and a overwrite kill-switch in case of emergencies. The laser beam exposure is controlled using a beam shutter.

3.3 Automated Probing

Before attempting to modify the resistive properties of Josephson junctions, it is essential to posses the ability to accurately characterize the resistance property itself. This is where the automated probe station (APS) comes into play. Figure 11 shows a schematic design of the operation hardware used in

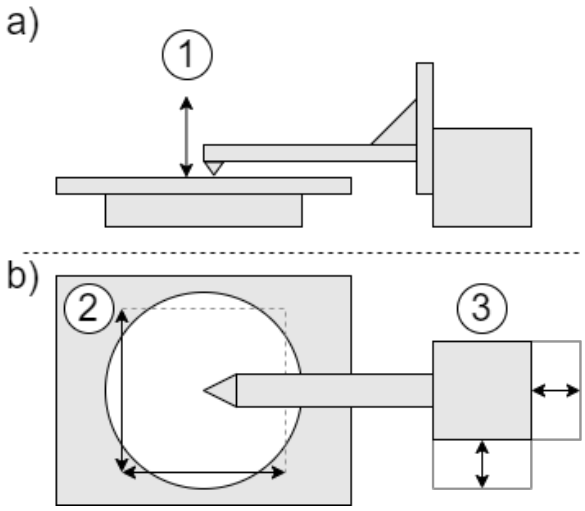

Figure 11: **Schematic Interpretation of Automated Probe Station**. a) Side-view of landed probe needle on the XY-stage which holds the 4 inch wafer using vacuum. 1) The vertical degree of freedom which can be controlled using the Thorlabs standardized APT driver. b) Top-view indicating the reachable range on the wafer. 2) Translation indicator of the motorized XY-stage (110 by 75 mm), which can be controlled using Thorlabs standardized APT drivers. 3) Manual XYZ-stage control for fine-tune of the vertical probe (only used once for system calibration).

the automated probe station. The horizontal XY-stage, used to mount and control the probing position on the wafer has a maximal travel speed and acceleration of 250 mm/s and 2000 mm/s respectively. The backlash, a unit for drift in position due to repeated back and forth motion, is not available for this stage. Mainly because the number is insignificant compared to the incremental movement precision of 0.1 μm.

The vertical translation stage (Z-stage), used to control the probe needle height, has a maximal travel speed of 2.6 mm/s but should be limited to 2.3 mm/s to prevent target-height distortion resulting from the acceleration profile. The known backlash of this component can reach up to <8 μm which is one order of magnitude lower than the advised landing depth. The landing depth is an additional lowering distance after the point of contact to make sure all four needles are properly touching the NbTiN. The probe

needles can tolerate a landing depth of 200 to 300 μm. This value is obtained from extensive testing on NbTiN contact pads. Traveling past the tolerated landing depth may cause the tungsten probe needles to bend beyond their elastic limit.

The motorized XY-stage and motorized Z-stage are controlled by an auto-alignment controller[10] and K-cube controller[11] respectively. Both work in combination with the Thorlabs APT control software. Which allows seamless integration into the main labview program.

The four probe needles are connected to a coax matrix box which allows the user to control if the individual coax cables should share a common ground or not. In the case of two-point measurements, the outer two probes (labeled 1 and 4) are connected to a so called junction measurement box. Which acts as a current to voltage converter with the use of a trans-impedance amplifier. The measurement box applies a static voltage of 10 mV over the two outer probe needles. The voltage drop over the squid-loop resistance and the combined contact resistances result in a current that feeds into the amplifier. The amplifier resistance is chosen such that the voltage output ratio ($1\text{V} : 10^3\,\Omega$) can be interpreted as conductance in μS. This output voltage is measured by a keithley multimeter and can be read out by labview using the VISA resources[12].

3.3.1 Circuit Design

The transmon resonance frequency is indirectly dependant on the critical current that describes the Josephson energy. This current is proportional to the tunnel barrier resistance at cryogenic temperatures. Probing this resistance at room temperature is important for characterizing the non-linear inductor component of the transmon. In our case, this component consists of a Josephson junction-pair in parallel. In order to understand the necessity of a 4-point resistant measurement setup, it is best to first explain the concept of a 2-point setup. Figure 12 is the circuit schematic used to implement both the minimal required setup (2-point) as the extended resistance measurement setup (4-point).

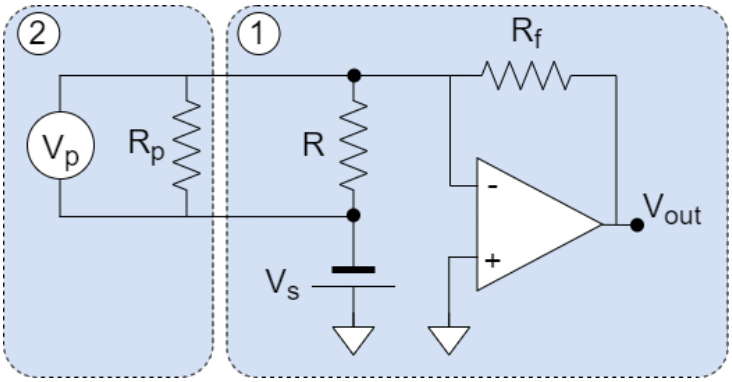

Figure 12: Schematic interpretation of 2-probe (4-probe extended) measurement circuit. 1) minimal requirement for 2-point setup using an operational amplifier with feedback resistor. 2) circuit extension required for 4-point setup using an isolated high-impedance differential amplifier (V_p). R is the junction-pair of interest which will be characterized. V_s is the voltage source applied to R. V_{out} is the voltage output of the opamp with R_f as feedback resistor determining the gain. R_p is a parallel resistor to R, which prevents a voltage difference built-up coming from V_p when circuit 1 and 2 are separated.

The Josephson junction-pairs have a resistance in the order of 10 kΩ. Standard resistors with these values can be characterized using an ordinary I-V approach, where one applies a current and measures the voltage drop over the resistor. The nano-scale nature of a Josephson junction however, introduces a significant restriction on this approach. Relatively high amounts of current can 'burn' a junction, destroying the tunnel barrier and shorting the circuit. Therefore, it is recommended to utilize a voltage source when working with Josephson junctions. The voltage source V_s in figure 12 is in the order of 10 mV, creating a current through the junction of the order of 1 μA. The current through the junction-pair

[10] APT NanoTrak®Auto-Alignment Controller
[11] K-Cube™ Brushed DC Servo Motor Controller
[12] Virtual Instrument Software Architecture, API developed by National Instruments.

is given by:

$$I_s = \frac{V_s}{R}, \tag{22}$$

where V_s the voltage source and R the substitute resistance of the measured component. Panel 1) illustrates the operational amplifier (op-amp) which acts as an inverting amplifier given by:

$$V_{out} = -I_s R_f = -\frac{R_f}{R} V_s, \tag{23}$$

where R_f the feedback resistor. The current induced by the applied voltage source is matched by the amplifier to create a virtual ground after the substitute resistor. By setting the feedback resistor value, the gain over the output voltage can be controlled. In reality however, the contact impedance of the probe needles are non-zero. This can be accounted for by replacing R with $R^{'} = R + 2\,\delta R$, where δR is the contact resistance in series with the junction-pair resistor R. The new expression for the current and the output voltage are given respectively by:

$$\begin{aligned} I_s^{'} &= \frac{V_s}{R^{'}} = \frac{V_s}{R + 2\,\delta R}, \\ V_{out}^{'} &= -I_s^{'} R_f. \end{aligned} \tag{24}$$

Using the 2-point measurement setup, the junction-pair resistance is now given by:

$$R = -\frac{V_s}{V_{out}^{'}} R_f - 2\,\delta R, \tag{25}$$

where $-V_s/V_{out}^{'} \geq 2\,\delta R/R_f$. A constant offset in characterization due to contact resistance is not necessarily a problem. It is still possible to quantify yield and fabrication control using a 2-point measurement setup. However, contact resistance becomes an issue when it varies per measurement. This is the case with the current setup, where the probe needles are continuously raised and landed to perform multiple measurements. To compensate for the contact resistances, the measurement circuit is extended by adding an isolated high-impedance differential amplifier connected to two additional probe needles (see panel 2 of figure 12). The high input impedance effectively neglects the contact resistances. The parallel resistor R_p is chosen to be 10MΩ, which is three orders of magnitude higher than the expected junction-pair resistance. Given that $R_p \gg R^{'}$, the high-impedance amplifier voltage is given by $V_p \approx I_s^{'} R$. Together with equation 24, the relation for R, independent of the contact resistances is given by:

$$R \approx \frac{V_p}{I_s^{'}} = -\frac{V_p}{V_{out}^{'}} R_f, \tag{26}$$

where $-V_p/V_{out}^{'} \geq 0$. Note that the high-impedance amplifier alone is not enough to determine the resistance. $V_{out}^{'}$ is still required to determine the current $I_s^{'}$ through the total resistance $R^{'}$.

3.3.2 Probe Needles

This experimental setup utilizes off-the-shelve probes from Cascade Microtech (FormFactor). They allow for customized probe designs based on the users requirements. For the purpose of measuring the resistance/conductance of Al/AlOx Josephson junction-pairs connected to NbTiN contact pads, the probe is equipped with 4 tungsten needles, separated by 40, 70 and 40 μm each.
Figure 13a shows a standard configuration. The probe needles are connected to ceramic blades which sit on a common ground plane. The brass-plate at the back of the probe head is mounted to the motorized-controlled probe-arm (see figure 11). A custom designed, 3D printed cover piece can be seen in figure 13b. In order to reduce the risk of damaging the needles during maintenance, this cover piece is placed on top of the probe head and fastened to the brass-plate. It is designed is such a way that it can be connected to the probe head from the moment it is transported out of its casing to the moment it is mounted on the probe-arm.

3.4 Device Alignment

Alignment is an essential part of the setup as it allows for sub-micron precision in locating device features, landing probe needles and directing the focused beam spot. Each device is interpreted as a two dimensional surface for which two non-parallel vectors can be used to describe any point on the surface.

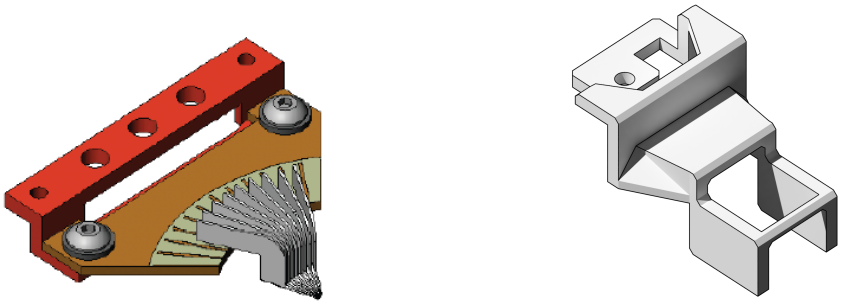

(a) (b)

Figure 13: **DCQ Probe Head & Cover**. Probe head example (a). Note, our probes host 4 neeldes instead of 9. A custom developed, 3D printed probe-head cover (b) to reduce the chance of damaging the probe needles during maintenance.

The normal vector of the XY-stage is aligned with the optical axis of the CCD-camera . The live video feedback is overlaid with an alignment grid which is used to precisely locate markers on a device. Each device is equipped with a minimum of three markers that are used to construct a transformation matrix between the motorized XY-stage and the device feature space. A generalized protocol is used to store and reference specific device-feature locations. All of this data is accessible to the user through a compact interface.

3.4.1 Marker Calibration

These markers are specifically placed to facilitate alignment not only for this process but also within other steps of the fabrication cycle. In order to define a complete transformation matrix, the three markers need to be mapped to their respective coordinates spaces on both the XY-stage offset and the device design. The solution vector $\vec{v}$ is constructed based on the marker coordinates $\{\vec{a}_1, \vec{a}_2, \vec{a}_3\}$ and $\{\vec{b}_1, \vec{b}_2, \vec{b}_3\}$ for the stage- and design-space respectively. Where the solution vector is given by solving all six linear equations:

$$\vec{v} = M\vec{n} = \begin{bmatrix} 1 & 0 & b_{1x} & 0 & b_{1y} & 0 \\ 0 & 1 & 0 & b_{1y} & 0 & b_{1x} \\ 1 & 0 & b_{2x} & 0 & b_{2y} & 0 \\ 0 & 1 & 0 & b_{2y} & 0 & b_{2x} \\ 1 & 0 & b_{3x} & 0 & b_{3y} & 0 \\ 0 & 1 & 0 & b_{3y} & 0 & b_{3x} \end{bmatrix} \begin{bmatrix} a_{1x} \\ a_{1y} \\ a_{2x} \\ a_{2y} \\ a_{3x} \\ a_{3y} \end{bmatrix} = \begin{bmatrix} D_{00} \\ D_{01} \\ D_{10} \\ D_{11} \\ c_0 \\ c_1 \end{bmatrix}, \tag{27}$$

where the elements of the solution vector can be used to construct the linear transformation from any design-coordinate $\vec{b}_i$ to corresponding stage-coordinate $\vec{a}_i$:

$$\vec{a}_i = D\vec{b}_i + \vec{c} = \begin{bmatrix} D_{00} & D_{01} \\ D_{10} & D_{11} \end{bmatrix} \vec{b}_i + \begin{bmatrix} c_0 \\ c_1 \end{bmatrix} \tag{28}$$

The stage-marker coordinates are obtained using a CCD-camera in combination with an alignment overlay. The design-marker coordinates can be given manually to the program during alignment, or they can be specified in the *device-protocol* data container.

3.4.2 Device-Protocol

This data container is used to store relevant device coordinate information and measurement method. It acts as an interface between the control logic and any arbitrary device layout. This allows the rest of the program to be device independent.

3.1: Device Data Container

Class constructor:

- ***Capacitor positions***, an array-like containing probe-landing positions.
- ***Squid positions***, an array-like containing annealing positions.
- ***Marker positions*** (optional), a three-element tuple containing alignment marker positions.
- ***Index pointers*** (optional), an array-like containing indices that correspond to *capacitor position* elements. Provides freedom over traversing order. Duplicate indices mean the same junction-pair gets measured multiple times.
- ***Index labels*** (optional), an array-like containing labels that correspond to *capacitor position* elements. Mainly used for data-analysis. Unique labels for unique indices.

The capacitor and squid positions are stored as absolute coordinates which use the same coordinate system as the markers. The decision was made to store both positions separately even though they are part of the same transmon layout. This is because not all transmons are oriented the same way and their design might even change in future iterations. The index pointers provide complete freedom over choosing which transmons to be measured in what order and how many times. These pointers also act as the backbone for mapping the output measurement data (see 3.6.1). The class constructor currently requires a manual input for each position coordinate. However, limited support for mapping directly from the PyQIP chip class[13] is already implemented. In the future this will remove the need to construct the device-protocols by hand.

3.4.3 Landing Calibration

In the idle state, the probe hovers above the device. Before measuring, the probe is lowered by the automated motorized Z-stage until the four needles make contact with the device. Deciding whether the probe has landed is done through both a visual and measurement feedback. The visual feedback is based on the CCD-camera which shows the needles pressing down on the device. This creates an elastic deformation in the tungsten needles, indicating the needles are no longer floating mid-air. The measurement feedback consists of a current passing through the device material upon landing the needles. Which gets measured by a 4-point measurement setup. The current flow is enforced by the voltage difference between the two outer needles. This form of feedback is only reliable if the contact material that connects the two outer probes conducts.

The landing height (or depth depending on perspective) is recorded for at least 4 points on the device to create a first order height map. The maximum empirically observed height difference between any two locations on a surface-17 device ranges between 20 or 40 μm. This range increases when considering wafer-scale devices and is likely due to the XY-stage not being perfectly level. These height differences can however easily be compensated by the elastic deformation range of the probe needles themselves, which can handle up to 300 μm displacement[14] in the direction of the surface normal. Meaning that the 'lowest' point on a given device can be chosen as landing height without having to consider a unique device-dependent height map. As for the hovering height, this is chosen to be 200 to 300 μm above the 'highest' point on the device in order to provide clearance for 3D features such as wire-bonds and air-bridges.

3.4.4 User Interface

Specifying the above mentioned alignment settings is done through a user interface panel withing the control software. Figure 14 is a highlighted version of this panel, giving a complete overview of all variables and their description.

The first highlighted section (1) shows the optical feedback of a device under an objective lens. The grid overlaid on the camera image serves three purposes: indicating the center of the screen for marker alignment, indicating the 4-point probe needle positions for landing (right-side) and indicating the center of the beam spot for annealing (left-side). In order to improve ease-of-use, the screen is made

[13] This is a design class which is used to produce .gds codes. Most fabrication processes are based on this format.

[14] This elastic deformation range is based on a NbTiN contact surface. Using other materials as contact surface, such as aluminium, will results in a different elastic displacement range.

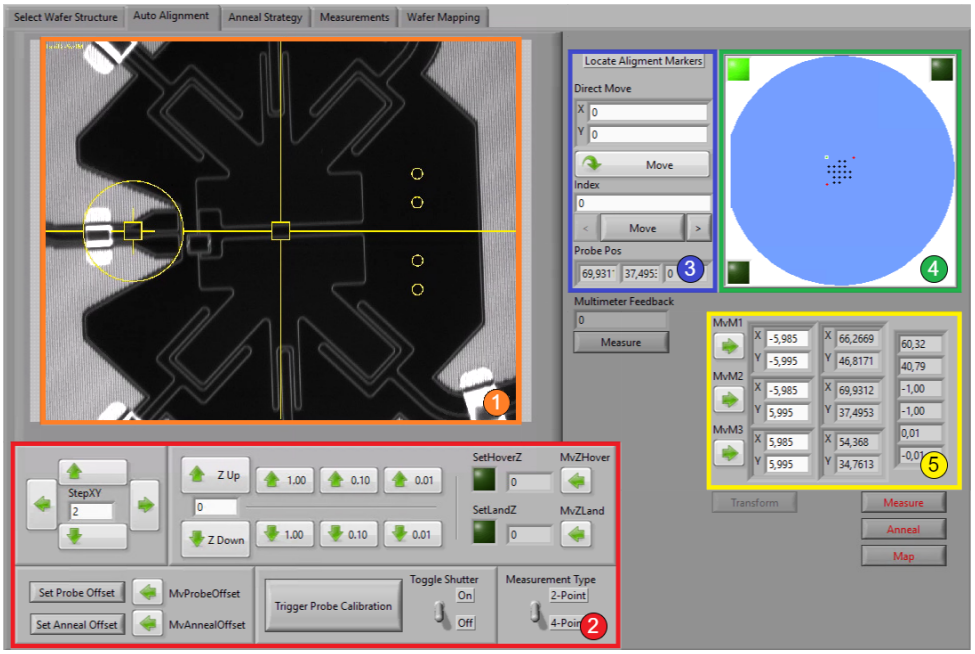

Figure 14: **User interface panel - Device alignment**. **1)** The main focal point of the device alignment is based on the optical feedback through the CCD-camera. **2)** Control panel for manually moving the XY-stage and Z-stage with fixed or adaptable step sizes. **3)** Quick navigation panel for moving to specific XY-stage coordinates or device coordinates based on a specified index pointer. **4)** Animated overview of selected device-protocol with red dots indicating the marker positions and black dots indicating transmon positions. **5)** Front-end option to specify marker locations in device coordinate space and the corresponding indicator for XY-stage coordinates as well as the transform matrix solution vector.

interactive. This allows the user to perform fine XY-stage positions adjustments through the click-and-drag functionality of the mouse. In addition to the xy- and z-control, section 2) contains the option of recording the landing and hovering heights for the Z-stage as well as applying an overhead offset to the probe and beam spot positions with respect to the center of the screen. This is especially important to prevent the probe needles from blocking the laser beam during annealing. These additional offsets also add flexibility in adjusting probe and beam spot positions without having to update the back-end protocols. For debugging purposes, this section also controls Z-stage calibration, beam-shutter toggle and whether to measure using a 2-point of 4-point measurement setup. Section 4) is a graphical overview of the selected device-protocol layout. The large circle represents a 4-inch wafer for scale. After setting all three marker locations, indicated by the three squares, the front panel updates and gives the possibility of recalculating the solution vector (see 3.4.1). The XY-stage has a limited range of motion which is known by the control software. Whenever the device is placed and aligned in such a way that some of the device features lay outside the physical reachable space of the probe, they turn red on the graphical overview.

3.5 Active Feedback

To achieve the goal of targeting transmon resonance frequency down to sub-50 MHz accuracy, thermal annealing can be used as a post-fabrication process that aims to increase the Josephson junction pair resistance in a controlled manner. In turn, decreasing the transition frequency of the transmon. This process depends on a number of factors including the surface area and thickness of the tunnel junctions as well as the incident laser power density and exposure time. Because each fabricated junction is unique [43], the thermal annealing process is tailored to each individual junction pair. This can be achieved by repeatedly measuring the change in resistance for each junction pair in between laser exposure. Active feedback annealing is an iterative approach where each junction pair is subjected to an alternating cycle of measurements and laser exposure, with the objective to move the total junction pair resistance to a predefined target. For a full description of the active feedback algorithm, see section 2.4. During each cycle, prior measurements are used to construct a profile for each junction pair, which is used by the

algorithm to predict the next round of exposure times.

3.5.1 Anneal-Protocol

This data container is used to interpret a range of exposure commands that are enforce on a device. At the basics, the thermal annealing system is only controlled by the exposure time and the power of the laser. Since the power is controlled manually (due to safety regulations), the exposure time is the main variable at play. However, when talking about resistance tuning, time is not a proper reference unit. Instead, this protocol allows the user to specify commands like: *target resistance* or a *fixed increase of resistance*, without having to specify the time required. The protocol is tasked with converting these commands to an exposure-time unit during the experiment.

3.2: Annealing Data Container

Class constructor:

- ***Anneal stamp***, an array-like containing value-token tuples. Each value is accompanied by a token which dictates how the value should be interpreted. For example,
  'default': (default token) no exposure required, ignore value.
  'delta_time': elapse time without exposure, value in [s].
  'expose_time': elapse time with exposure, value in [s].
  'target_res': target resistance, value in [MΩ].
- ***Annealing statistics*** (optional), a system-output data wrapper that holds prior annealing results as an initial guess for converting target-resistance tokens into predicted exposure time tokens.

The array of value-token pairs does not have to be the same length as the index pointers array from the device data container (see 3.4.2), instead it is used as a stamp which repeats until all indices are appointed a corresponding value-token pair. This makes sure that both data containers do not depend on each other and can in principle be used to mix and match different protocols.

3.5.2 Annealing Statistics

The annealing data container also allows for an optional second constructor parameter. This parameter is used as an initial guess to predict junction-pair annealing-behaviour based on earlier obtained annealing statistics. In the absence of prior measurement data, the active feedback cycle can use these statistics to form an initial annealing-behaviour profile. Annealing statistics is collection of experimental data that describes the change in junction-pair resistance depending on exposure time with a set laser power density. Figure 15 shows three groups of junction-pairs. Each group consists of junctions with designed width ranging from 70 to 170 nm. Each group is thermally annealed at their respective laser power ranging from 2.7 to 30.2 mW. Note that the data at 2.7 and 5.1 mW is collected using the outdated 2-point measurement setup, while the data at 30.2 mW utilizes the improved 4-point setup. Since the beam spot is held constant during each measurement, the labels refer to (post-optics) laser power instead to power density. Even though the current setup is able to comfortably reach 300 mW of power, no statistics has yet been obtained from anything higher than 30 mW due to the limited number of identically fabricated test-devices. Comparable to prior research [16], the change in resistance is observed to have a power-law-like dependence on exposure time. In order to fit this dependence, section 2.4 introduced the fit-function $f_{\alpha,\delta}(t) = \alpha t^{1/\delta}$ which is used to fit the annealing-behaviour. Table 1 demonstrates the obtained fitting

Power [mW]	Elapsed Time [s]	α [10^{-2}]	δ	Data Points
2.7	120	0.072	1.375	45
2.7	270	0.115	1.597	90
5.1	50	0.343	1.678	144
5.1	350	0.726	2.636	288
30.2	60	4.283	4.640	19
30.2	150	2.964	3.626	35

Table 1

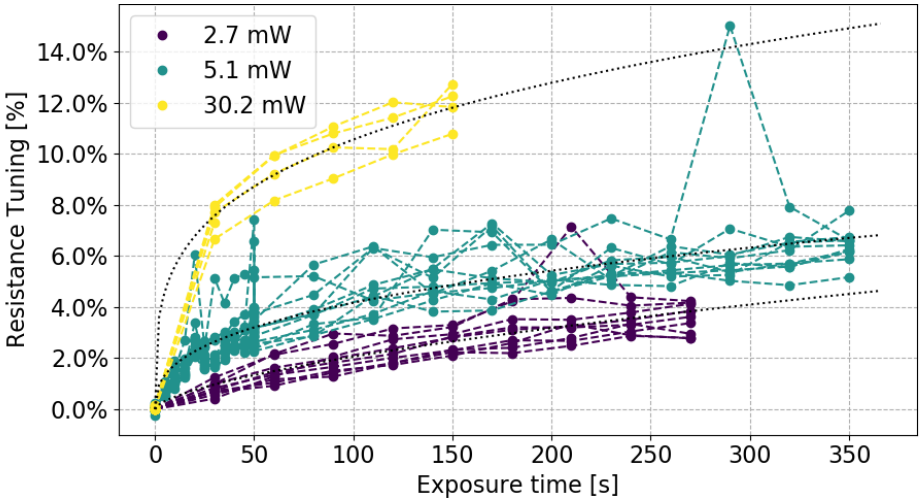

Figure 15: **Annealing Statistics**. Iterative resistance measurements under periodic laser exposure at various power settings. The percentage change in resistance compared to the starting value is recorded over an interval of open-loop exposure times. Note that the data at 2.7 and 5.1 mW is collected using the outdated 2-point measurement setup, while the data at 30.2 mW utilizes the improved 4-point setup.

parameters for different laser power settings. A common way to argue the reliability of a time-dependent fit, is to compare the fit parameters of the complete set of data points to the time-truncated set. This indicates how well the fit parameters obtained from the time-truncated data set is able to predict the complete data set.

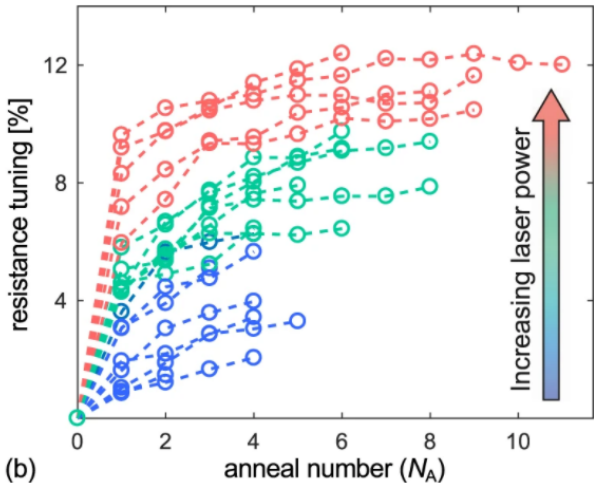

Figure 16: **Annealing Statistics IBM**. "Adaptive anneal progression towards target resistance in 20 tunnel junctions." (Source: [16]). The colors blue, green and red correspond to laser powers 1.74, 1.85 and 1.96 W, respectively. Each anneal iterations (x-axis) corresponds to ∼0.3-8 seconds. Total duration's: ∼8-22 seconds.

The obtained behaviour can be compared to literature. Figure 16 comes from a 2021 paper from IBM on laser annealing of Josephson junctions. Their setup utilizes a test device with 36 fixed-frequency transmon qubits. Each transmon consists of a 100 by 100 nm Al/AlOx Josephson junction, in between two 500 by 320 μm planar capacitor plates. Note that their annealing protocol is vastly different than ours. They utilize a diffractive beam splitter to create a four-spot beam pattern, to avoid direct illumination of the junctions. Meaning they effectively heat up the silicon substrate and indirectly anneal their junctions. Our setup on the other hand, targets the junctions directly. This explains the order of magnitude power difference between the two experiments. Nonetheless, their observed evolution of annealed junctions under iterative exposure times is comparable to the results in figure 15.

3.6 Class Structure

3.6.1 System Output

This data container is used to store experimental data together with all relevant settings and protocols used during an experiment. It acts as an all-in-one package with an extensive property-interface. This interface is mainly used for data-analysis and plotting purposes.

3.3: Output Data Container

Class constructor:

- ***Measurement cluster***, an array-like containing four-element tuples. Each tuple consists of an index pointer (i), capacitor position ($\vec{p}$), measured conductance value (v) (in [μS]) and exposure value (t) (in [s]). These tuples are stored in the order of execution, which depends on the order of index pointers within the wafer-protocol class:

$$\begin{matrix}(i_0,\, \vec{p}_0, v_0,\, t_0)\\ (i_1,\, \vec{p}_1, v_1,\, t_1)\\ (i_2,\, \vec{p}_2, v_2,\, t_2)\\ \vdots\end{matrix} \tag{29}$$

- ***Wafer protocol***, a device-data-container used during the experiment.
- ***Anneal protocol***, an annealing-data-container used during the experiment.
- ***Meta-data*** (optional), a dictionary-like containing additional information such as measurement completion time, experimental description, etc.

The wafer- and annealing protocols mentioned in the class constructor are the exact same interfaces as described in section 3.4.2 and 3.5.1. The output data container wraps those containers together with the obtained measurement data and some additional meta-data.

3.6.2 Properties

The access properties of the system-output class solely consists of *getter*-functions. This ensures that the raw data is not exposed to any changes during data-analysis. Besides the basic raw-data access, there are specific key-value getters that link the unique index pointers (junction-pairs) to higher-level information. This includes:

- Position on the device.
- Identifier label (e.g. 'D9', 'Z3', 'X1', ...).
- Sorting label-index (e.g. 'D1': 0, 'D2': 1, ..., 'D6': 16)
- Chronological measurement data obtained throughout the experiment. (Both 2- and 4-point)
- Chronological exposure time applied throughout the experiment.
- Whether the junction-pair is part of a control group.

In the context of laser annealing, a control group consists of junction-pairs that receive no laser exposure during an experiment and are used as reference, or to study proximity annealing. Where proximity annealing refers to the phenomenon of unintended thermal annealing to junction-pairs that are spatially close to the targeted junction-pairs. The system-output class allows for setting a sorting dictionary that does nothing more than specify an index for each junction-pair label. This is useful for plotting data in a consistent order, irrespective of the traversal order during the experiment. Consequentially, the label-sorter and control-group-identifier properties are the only exceptions that have their own setter-function.

3.6.3 Build-in Plotting

An important part of performing experiments is the data-analysis that follows afterwards. To ensure clarity and uniformity, each plotting functions utilizes the same function template:

```
def plot_function_name(data: ISystemOutput, **kwargs) -> matplotlib.pyplot.axis:
    """
    Returns static axis plot. **kwargs arguments are applied to axis.
    """
```

The consistent structure of the system-output interface ensures backwards compatibility to all plotting functions that are constructed using this template.

3.6.4 Data Organization

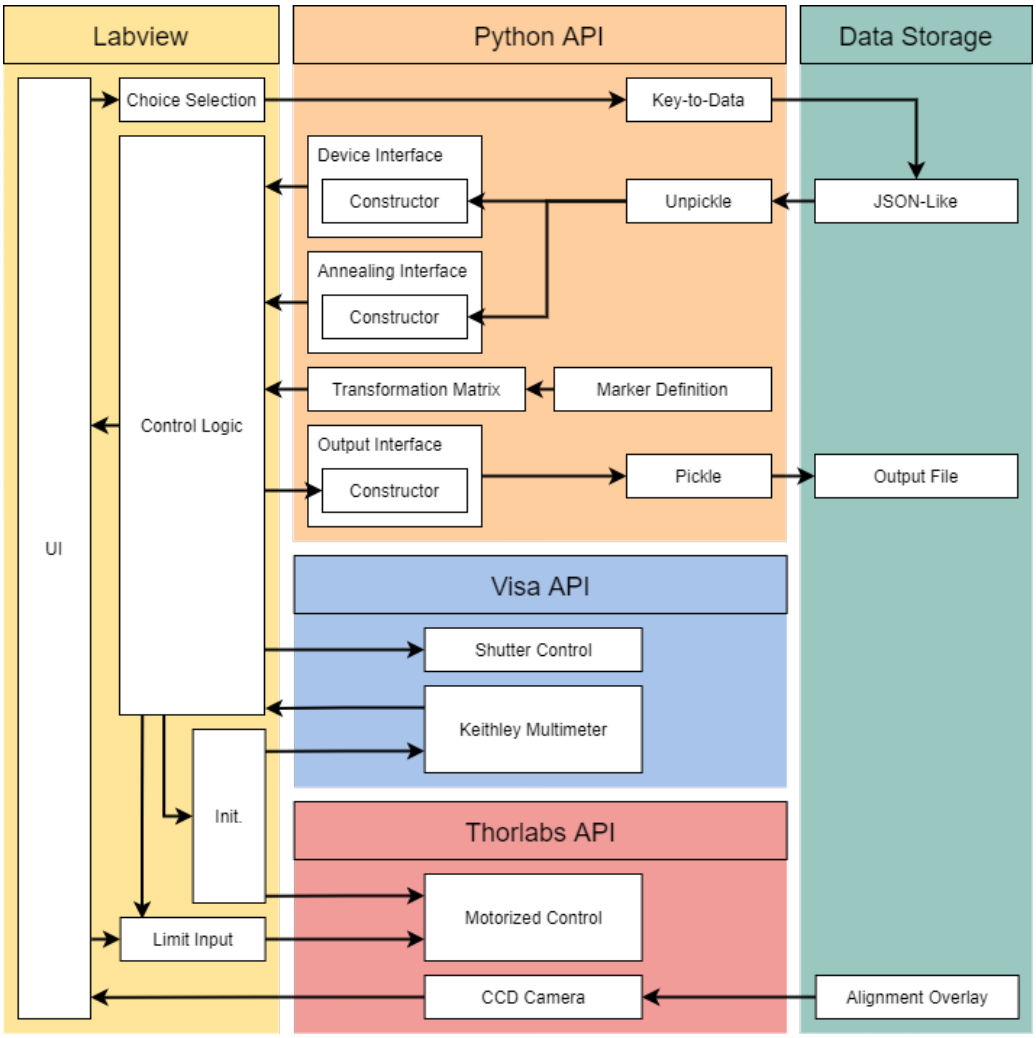

Figure 17: **Simplified Data Flowchart**. Showcases the main environments that are involved in this system. Left) Labview hosts the user interface and manages communication to and from the different API's through the control logic. Center) The python API manages data storage and retrieval, together with formatting data to feed to the control logic. Both Visa and Thorlabs API's are used as a connection to the respective hardware controllers. Right) The data storage footprint.

Figure 17 provides a simplified overview of the data flow between all communicating modules. The user interface (UI), located on the left of the image, encapsulates the entire interaction between the user and the system back-end. This includes initializing, sending and receiving commands to and from hardware controllers such as the motorized XY-stage and Z-stage as well as the beam shutter and Keithley multimeter. Labview is used as mediator between the UI, python back-end and hardware controllers. It

therefore hosts most of the control logic for running experiments. The remaining part of the logic is performed by the python back-end because it is easier to maintain and allows for better generality. In the future the current labview environment will be subdivided and replaced by a python front-end, together with a python control-logic module. This will also improve the overall test-ability of the system which is currently limited to the python back-end.

The python back-end (labeled python API) is responsible for interpreting the choices made by the user through the UI. It is able to read and write data from storage. It utilizes a custom class that makes it easy to serialize complex class objects to and from a JSON-like file structure[15]. All classes that contain experiment data inherit from this serializable parent object.

[15] Pickle is a python library that deals with object serialization. It is a plain, non-encrypted serialization method.

4 Results and Discussion

4.1 Sample Devices

Throughout this section there are two main device series used. A prototyping device series named 'Blackbird' and an official surface-17 device series named 'Prometheus'. The Blackbird series is prioritized for whenever large statistics is preferable as each of these devices host 272 test-pad junction-pairs (see figure 19b). These test-pads are specifically designed to test the transition between 2-point to 4-point measurements. The 272 junction-pairs are grouped in 17 groups of 4-by-4 arrays, where each array is part of one of three design groups: 'low', 'medium' or 'high'. Similar to the three frequency groups for a surface-17 device. Corresponding to their group, each array hosts a range of designed junction widths. The bottom electrode is varied corresponding to the design groups; 'Low': 60 to 120 nm, 'medium': 112 to 168 nm, 'high': 168 to 228 nm. While the top electrode width is fixed at 160 nm. The design width determines the conductance value for each junction in a pair.

The Prometheus series is as close to the official quantum processor devices as possible. It includes 17 transmons in a surface-17 layout (see figure 18a) and hosts the full set of out-of-plane airbridges. The latter is used by the newly developed PyCLQ program to not only verify airbridge placement but also quality using image recognition. These devices were used to quantify XY-stage performance in section 4.2.

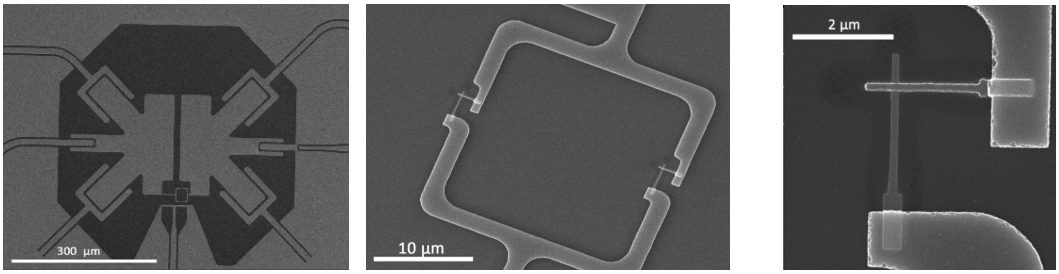

(a) (b) (c)

Figure 18: **Example Transmon Qubit** Transmon circuit (a), including SQUID loop, capacitor plates, flux-bias line, read-out resonator line and inter-qubit bus resonators. (b) The SQUID loop. (c) Al/AlOx, X-type (Manhatten) Josephson junction.

All devices used during the project were fabricated using X-type Josephson junctions as is seen in figure 18c. Which means all data collected is based on these junction designs. Considering the scope of this project and the potential future usage of the APS, it is important to be flexible regarding device layout. As discussed in section 3.4.2, the device-protocol allows for non-trivial device layouts. One example of this can be seen in figure 19a, which shows a wafer-scale test device including both junction-pair test-pads and VIA-markers. Because the layout of both these elements can change throughout development, it would be helpful to automatically update the device-protocol. Precisely for this reason the project python backend is equiped with an addon that allows the user to import and convert the original design code[16] of the *.gds file into a device-protocol class. This conversion takes into account the overlap of test-pads with, for example, VIA's. The converted device-protocol is aware of the test-pads which are potentially too close to VIA's and skips them during characterization. Functionalities like these are easily added or extended to the program. As a result, the system becomes much more accessible for the fabrication team which already use these *.gds files for design and fabrication.

[16] The Chip class from the PyQIP library.

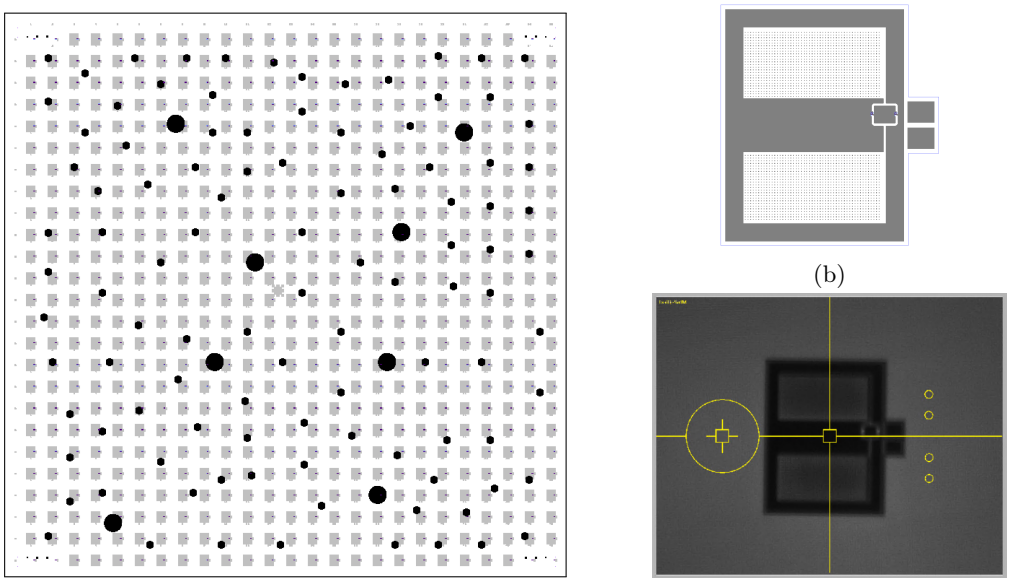

(a) (b) (c)

Figure 19: **Example Non-Trivial Test Layout** A non trivial device layout (a) with 621 test-pads (junction-pairs) arranged in a grid-like fashion, surrounded by virtual VIA's. (b) An enlarged version of the test-pad design. (c) A screenshot of a test-pad, taken from the CCD-camera point of view. Including alignment overlay.

4.2 Motorized XY-Stage Performance

A major benefit to automated hardware is the capability of performing fast, repeated and fine-controlled motions. For the laser annealing of sub-micron device features, consistency and repeatability are essential requirements. The high-speed motorized xy-stage, instructed by the corresponding benchtop controller, manages the device position during measurement and annealing. In order to quantify the performance of this stage we designed an experiment that utilizes the optical feedback of the CCD-camera together with a custom image recognition algorithm (PyCLQ) that is able to accurately determine device-feature locations.

The first experiment looks at the position drift of the motorized stage that accumulates overtime while continuously moving back and forth between predetermined locations. We decide to track four airbridges that are located roughly at the corners of the device (Prometheus). Airbridges are a common device feature and make for excellent 'land-marks'. This four-airbridge cycle ensures that the stage travels the same distance in both x and y coordinates. The prediction for this experiment is that the relatively large displacement per step ($\sim$ 10mm) should not result in any noticeable hysteresis in either the x- or y-direction, since the minimum incremental movement is claimed to be 0.1μm by the supplier.

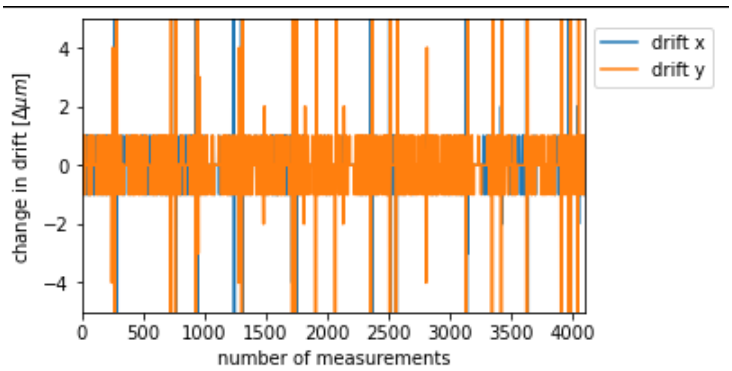

Figure 20: **Corner-to-Corner Test**. Calculated difference between designed and measured airbridge locations at four corners of the device at multiple rounds.

Prior to the experiment the device is aligned and a transformation matrix between the stage and device

coordinate system is constructed. For each iteration, the stage is moved to the next airbridge position defined by the device coordinate system. Once arrived at the correct position, the CCD-camera takes a snapshot which is feed into the image recognition algorithm. The algorithm locates the airbridge within the image. The accuracy in determining the location is limited by the image resolution ($\sim 1\mu$m). Figure 20 shows the difference in position derived from the algorithm and the designed position for each iteration. Each airbridge is visited 1024 times giving a total of 4096 iterations. We conclude no significant drift accumulating in either the x- or y-direction. The variation in the position difference can be explained by the image resolution. The outliers correspond to camera snapshots that are either blurry or otherwise not recognizable.

For the next experiment, the four selected airbridges are aligned on the same diagonal (following feedline Z1). In addition, the four airbridges are located at close proximity, roughly $\sim 280\mu$m apart. Figure 21 tracks the difference in position for the first and fourth airbridge in the sequence. Again,

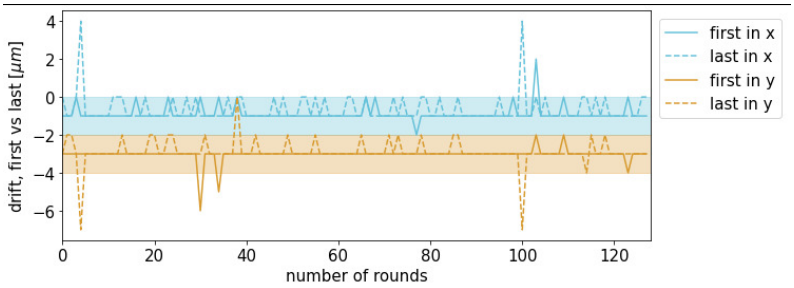

Figure 21: **Large & Small Skip Test**. Calculated difference between designed and measured airbridge locations for the first and last airbridge in each round.

there seems to be no significant drift accumulating in either the x- or y-direction. The mean in both axis however, are shifted by -1 and -3 μm respectively. This overall deviation can be explained by the misalignment of markers, which differs from the previous experiment, and thus the construction of an imperfect transformation matrix. Meaning there is a systematic difference in airbridge positions according to the device design file and the XY-stage coordinate system.

4.3 Measurement Statistics

In order to perform closed-loop laser annealing, it is necessary to probe the conductance of each junction-pair multiple. Here we describe the experiments performed using the automated probing part of the system. Up till now most devices are characterized by a single round of 2-point conductance measurements (see section 3.3). We have documented the observed deviation in measured conductance due to varying contact resistance. The following experiments aim to quantify this deviation and identify/solve potential problems that arise when dealing with a large number of junction-pair measurements.

The following experiment is performed using a Blackbird device (see section 4.1). The objective is to quantify the performance and consistency of measuring junction-pair conductance multiple times (up to 10 rounds).

Figure 28 demonstrates two tactics: a) Measuring each junction-pair ones in a random order before repeating the same process for the next round. b) Measuring each junction-pair 10 consecutive times, before moving to the next random junction until all junction-pairs are measured. This experiment shows a clear indication that the system has problems with maintaining the correct landing height. This problem is identified as the vertical Z-stage landing height drifting over successive rounds. A solution is adopted where the Z-stage re-calibrates every 50 or 100 measurements. This, together with the adaptation of a lighter probe-arm to reduce strain on the mechanical spring, results in significant performance improvements seen in figure 29:

Even though the measurement consistency improved and the three frequency groups are better distinguishable by their plotting colors, the variance in conductance measured is still unreliable high. This poses a problem when thinking about active feedback annealing where prior measurements are used to predict the conductance after thermal annealing. As described in section 3.3.1, here we upgrade the measurement setup from a 2-point to 4-point. The additional high-impedance voltage probes are used to distinguish the actual junction-pair resistance from the contact resistances imposed by the probe needles.

Figure 30 shows the resulting conductance probing using the upgraded 4-point measurement setup with additional Z-stage calibration. These procedures reduce the average standard deviation to 0.1 μS

conductance. If we consider the average junction-pair conductance of 200 μS, the current setup is able to determine the junction-pair conductance with 0.05% variation. Which would theoretically correspond to a 0.025% variation in targeting the qubit transition frequency f_{01}, assuming that we have the perfect understanding of how the junction-pair conductance translates to transmon resonance frequency. Considering a qubit at resonance frequency of 6.0 GHz, the readout variation is roughly 1.5 MHz. Understanding the readout variation is relevant in quantifying the lower-limit precision with which the tuning of junction-pairs to a target value can be achieved.

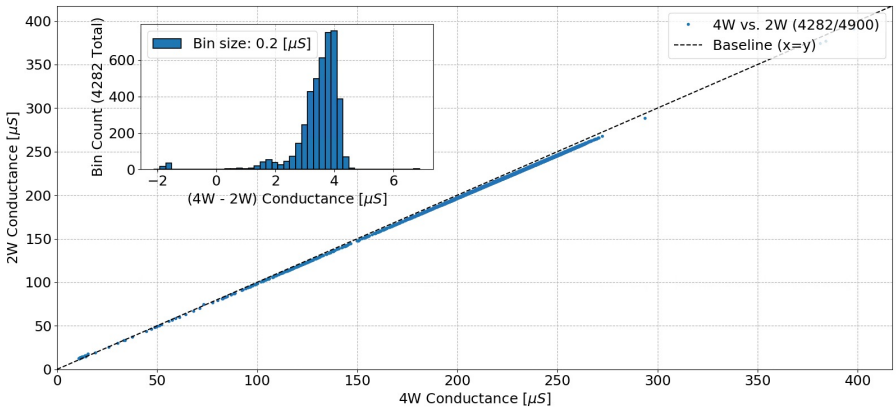

Figure 22: **Measurement Statistics 4-point vs. 2-point.** A baseline comparison between 2-point and 4-point measurements. From the 4900 junction-pairs present on the wafer, 618 are shorted and do not contribute to the plot. The inset histogram shows the difference between 2- and 4-point measurements over the entire dataset.

Another advantage of performing a 4-point measurement is that we can compare the two and see the contact resistance contribution. Figure 22 shows the comparison between 2- and 4-point measurements on a wafer-scale test device using 4282 junction-pairs. The diagonal line corresponds to the baseline: $x = y$. Each measurement is indicated as a single dot. Apparent is the agreement between 2- and 4-point measurements at low conductance (high resistance), while for high conductance (low resistance) a discrepancy starts to arise between the two measurement tactics. This can be explained by the fact that the 4-point measurement successfully filters the contact resistances which become significant at high-conductance junction-pairs. From the inset we can observe an average 4 micro Siemens difference between the two measurement tactics.

4.4 High Precision Resistance Tuning

With all essential systems working as intended, it is now possible to take any device containing Josephson junctions with contact pads and perform controlled laser annealing using an active feedback approach. The following experiment is a fully automated demonstration of this system's capabilities. To prevent any confusion, from this point on we will be talking about resistance instead of conductance as this is used in benchmark tests in prior literature. For the relation between a transmons resonance frequency and its inductive component resistance, we refer to section 2.2.1.
Figure 23 demonstrates one of the selective annealing experiments where a group of junction-pairs are exposed to thermal annealing under the guidance of the active-feedback algorithm (see section 2.4). With the objective of tuning these junctions to a fixed target resistance. During this experiment the exposure time is varied each iteration, while the laser power is set to a fixed value. As discussed in section 3.5.2, a number of open-loop laser annealing experiments have been carried out on a large ensemble of junction-pairs at different laser power settings. This data is used as an initial guess of how each junction-pair will likely react to their respective exposure. As the experiment continues, each junction-pair receives their own 'behaviour' profile. This profile is updated every time the junction-pair is annealed and measured. The active-feedback algorithm adjusts its decision making based on these profiles to improve convergence to the target resistance.

Besides the number of successful tuning events, the same figure also showcases potential limitations to the current system. In particular we want to highlight junction-pairs $X4_{1d}$, $Z1_{1d}$ and $X1_{4a}$. Where $X4_{1d}$ has a starting resistance of 5.9 kΩ while its target is set to 5.8 kΩ, a.k.a below starting value. This particular junction-pair did not reach its target due to the mono-directional tuning nature of this

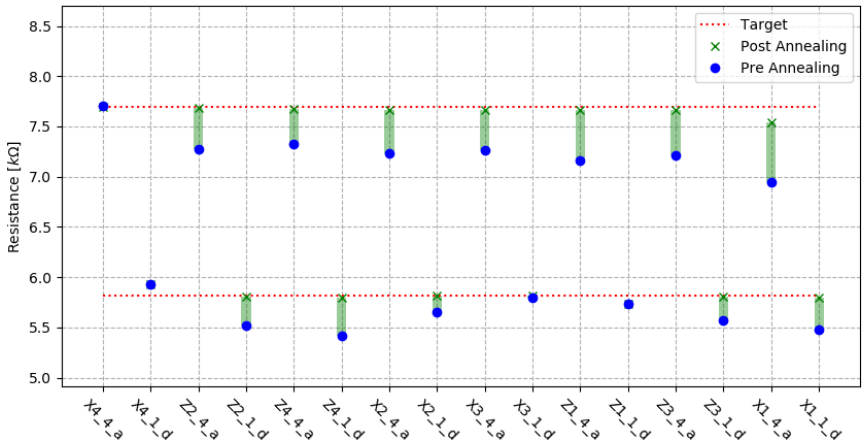

Figure 23: **Resistance pre- & post-Annealing**. 16 Individual junction-pairs, each with a semi-random starting resistance, divided in two groups. Both groups are tuned to their (arbitrary) target resistance of 5.8 and 7.7 kΩ respectively. Laser power: 30 mW, total exposure time: ≤300 seconds.

laser annealing setup. Finding a reliable way to both increase or decrease a junction resistance using laser annealing is an ongoing research topic and a potential solution is discussed in section 4.5. The post-annealing resistance value of both $Z1_{1d}$ and $X1_{4a}$ are a consequences of finite exposure time. As shown before, the percentage resistance change due to laser annealing seems to saturate at long exposure times. For $Z1_{1d}$, the post-annealing resistance is unchanged from its starting value because it was already subjected to a prior annealing test where it was exposed to the same laser power for 350 seconds. For $X1_{4a}$, even the full experiment duration time was not sufficient to tune the candidate on target. Instead, the resistance tuning seems to 'saturate' as predicted. Both this limitation are relatively easy to circumvent by increasing the laser power output, which increases the tune-ability range. Or by increasing the total experiment duration time, which increases individual laser exposure times.

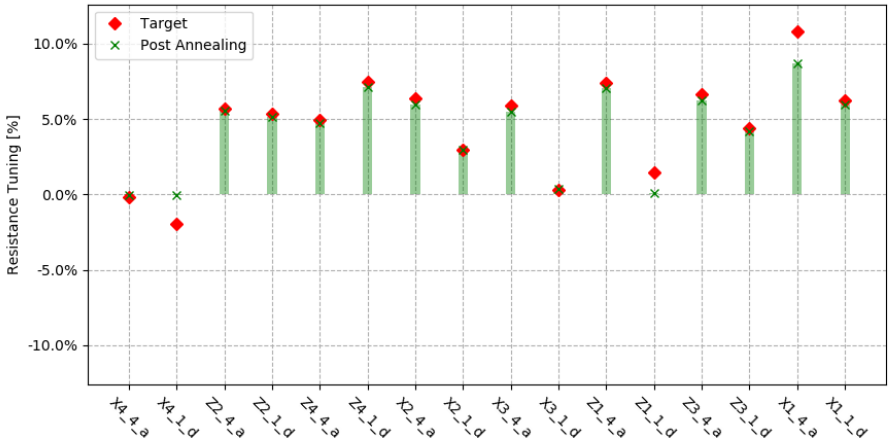

Figure 24: **Percentage Tuning**. Resistance tuning plotted in percentage with respect to the initial resistance.

Figure 24 represents the same data, but formulated using percentage resistance change with respect to the initial resistance. This makes the comparison with literature [5] more straightforward. In the referred paper, a maximum tuning range of 14% is achieved. Although the limitation for this tuning range is not specified. For our setup the maximum tunability range observed is 12%[17], which mainly depends on the laser power output and can easily be increased for future experiments.

[17] This 12% tunability range was observed in one of the open-loop annealing experiments, with laser power of 30.2mW.

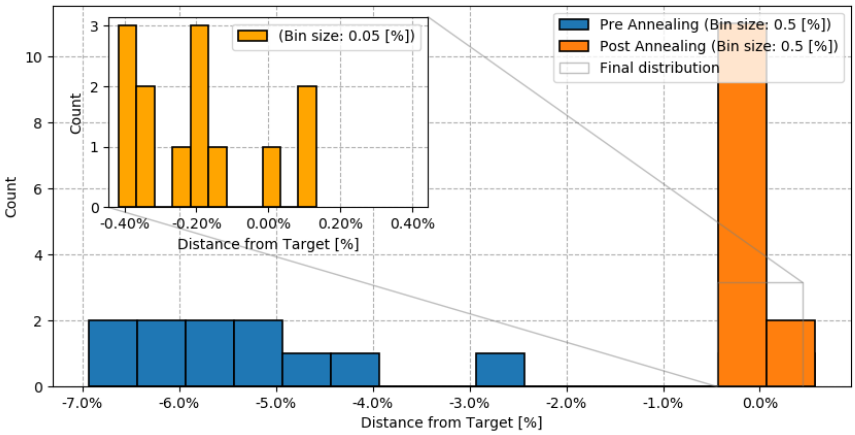

Figure 25: **Targeting Performance**. Histogram of the percentage difference between the target resistance and each junction-pair resistance before and after active-feedback annealing.

In order for this technique to be useful in frequency targeting, it is important to quantify the precision with which tuning to a target resistance can be achieved. Figure 25 shows a histogram of the above mentioned experiment. For clarity, this figure **excludes** the 3 earlier identified outliers ($X4_{1d}$, $Z1_{1d}$ and $X1_{4a}$). Simply because their contribution only highlights a flawed estimation by the experimenter, instead of a systematic limitation of the system. The histogram displays the 'distance from target resistance' distribution for all junction-pairs before (blue) and after (orange) active feedback annealing. As a rule of thumb, the distance from target resistance in $x\%$ corresponds approximately to a distance from target frequency in $\frac{1}{2}x\%$. This is due to their one-over-square-root relation (see section 2.2.1).

As seen from the figure, the maximum deviation before annealing was around 7% (3.5% in frequency). At an average qubit frequency of 6 GHz, this would translate to a deviation of 210 MHz from target. The figure inset shows the targeting precision after annealing of about $\leq 0.4\%$ ($\leq 0.2\%$ in frequency). Taking the same average qubit frequency, this would translate to a deviation of 12 MHz. Well in range of our sub-50 MHz objective. The active-feedback algorithm is biased towards undershooting the target resistance, meaning that the average targeting precision is 0.3% (0.15% in frequency). This of course assumes a flawless determination of the scaling factor M between the normal-state resistance and transition frequency.

A watchful eye would point out this only holds for $\leq$210 MHz deviations from target resistance and that larger deviation might not reach this targeting precision. To this we would like to point out that the tunability range depends mainly on the laser power density. This can be controlled either by the laser power output, which can achieve at least 10-times larger power outputs than shown in this experiment, or the beamspot diameter, which can be reduced by a more well defined optical system. The targeting precision on the other hand, is mainly limited by the variation in resistance measurement and the active-feedback method. Both of which are independent of the tunability range.

4.5 Potential Bi-Directional Solution

The current laser annealing setup operates by decreasing Josephson junction conductance through thermal annealing. This is a one-way process. The observation of decreasing junction conductance through either thermal annealing or idle over time is not new and is referred to as aging [44, 45]. The opposite effect, anti-aging, is also observed in literature [46]. Knowing that both processes can occur under the right circumstances makes it an enticing prospect as post-processing tool.

Personal speculation: An interesting distinction to make is that the act of thermal annealing is not what enables a junction to 'age', instead the aging process is accelerated by introducing energy into the junction structure. Similarly, if anti-aging is achieved by altering the atmospheric composition during thermal annealing, it implies that the (anti-) aging process is driven by forming chemical equilibrium. This equilibrium likely depends on both the junction composition and the surrounding atmosphere.

This experiment aims to reproduce the anti-aging effect in a controlled manner. Figure 26 shows 16

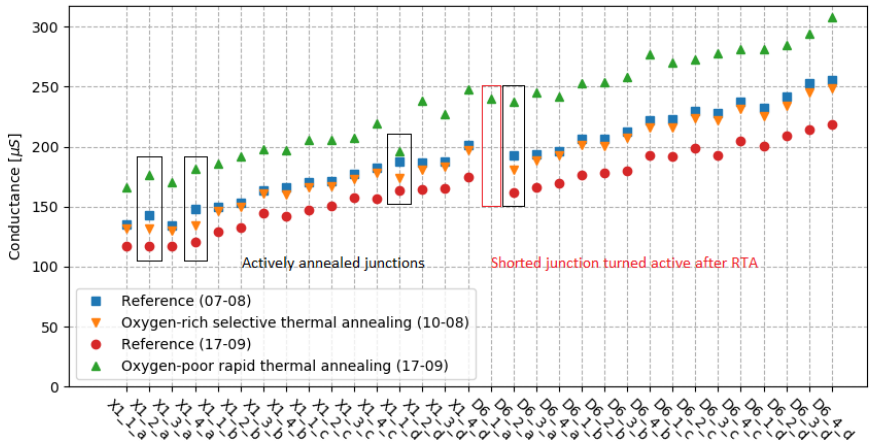

Figure 26: **Rapid Thermal Annealing**. Global thermal annealing in a forming-gas environment (90% N_2, 10% H_2) at 300°C for 120 seconds. An overall increase of conductance is observed for all junctions, irrespective of prior annealing. Note the revived junction pair at $D6_{1a}$ after RTA.

junction-pairs, indicated on the x-axis, in 4 different stages in time, indicated by the colors/shapes. This test device is intentionally the same as the one used for active-feedback annealing. This means that a number of these junctions have already experienced thermal annealing. The 16 junction-pairs are a subset of the total 272 junction-pairs. The squares represent the initial characterization after the test-device was delivered to the APS for the first time. Over the span of 3 days, a multitude of junction-pairs were targeted for thermal annealing to varies targets (highlighted by open black rectangles). The downward facing triangles show the complete characterization after the original thermal annealing experiments. Afterwards, the device was stored under normal cleanroom atmospheric conditions (no vacuum box). The circles represent a re-characterization after a month. During this time the device has experienced global aging, indicated by the reduction in conductance. The aging percentage depending on the junction design parameters is further explored in figure 27. The re-characterization is in preparation for the rapid thermal annealing experiment where the entire device is rapidly heated up to 300°C for 120 seconds, in a forming-gas environment (90% N_2, 10% H_2). As predicted, this results in anti-aging where the individual conductance of each junction increases across the entire device.

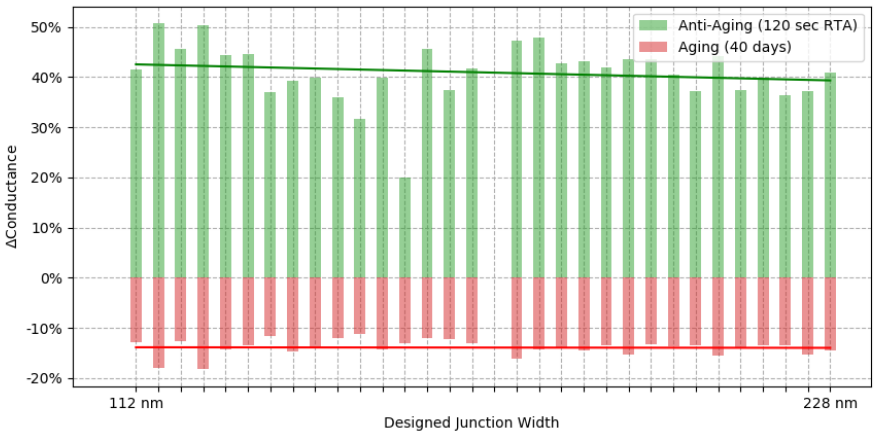

Figure 27: **Normalized Aging vs. Design Width**. Both the idle aging and active anti-aging processes are normalized based on the initial conductance which is proportional to the junction design parameters.

The upward facing triangles show the measured conductance after the rapid thermal annealing experi-

ment. Something that is not shown in the figure but most certainly the case, the rapid thermal annealing increased the conductance globally throughout the device. Additionally, the aging and anti-aging seems to be proportional to the individual junction conductance which is a function of their design width. In other words, small junctions experience less aging and anti-aging than larger junctions. Figure 27 shows a bar-plot of the normalized aging and anti-aging process based on the initial junction conductance. The data set is ordered based on the designed junction width. The first observation we make is the monotonic decrease in conductance, relative to the initial conductance due to idle aging. The second observation is that, for active anti-aging[18], the increase in conductance is less monotonic with some very distinct outliers.

Overall, incorporating anti-aging into our arsenal for fine tuning Josephson junction resistances is enticing. We have seen accelerated aging using targeted laser annealing and we have demonstrated anti-aging using global thermal annealing in a forming-gas environment. Together, these techniques could potentially open the door to arbitrary precision in frequency targeting post-fabrication.

[18] Where active anti-aging refers to applied thermal exposure using RTA, instead of an idle process.

5 Outlook

At the end of the project there are a number of topics worth improving or exploring. This section will give a concise overview of these topics, each with a description on how to move forward.

- **Focus beam spot**. As discussed extensively, the tunability range enabled by thermal annealing strongly depends on the laser power density applied to the Josephson junctions. Besides increasing the laser power output, it is valuable to decrease the beam spot area as much as possible. A possible improvement to the setup would be the addition of a collimating lens and concave lens duo between the periscope and dichroic mirror. This would provide the necessary control to minimize the beam spot size at the objective distance required for a focused sample image.

- **T_1 Coherence times**. The most crucial validation of this entire project would be to check whether frequency targeting by thermal annealing of Josephson junctions would compromise T_1 coherence times. The process to achieve this would involve, for example, a surface-17 device which is measured post-fabrication, cooled to operation temperatures and fully characterized (at least resonance frequencies and T_1 coherence times). Tuning corrections would be proposed based on the post-fabrication conductance measurements and measured resonance frequencies. The device would be warmed up, undergo active-feedback laser annealing and cooled down once more for final characterization.

- **Reduction in residual ZZ-coupling**. Once the previous test is successful and the effect on T_1 is acceptable, it would be possible to create a model that would automatically produce target frequencies (resistances) for active-feedback tuning. Not to achieve text-book frequency targeting, but instead to optimize the qubit frequency distribution on a device to minimize residual ZZ-coupling.

- **Bi-directional tuning**. Only briefly touched upon during this project, bi-direction tuning would create a much more forgiving environment for fabricating high-quality devices. This would therefore increase the total acceptable device yield. From the single test performed at the end of this project, bi-directional tuning does not only seem possible, but arguably feasible. A further study on the influence of temperature, atmospheric composition, exposure time and chemical decomposition of Al/AlOx Josephson junctions is suggested to better understand the processes that drive (anti-)aging. Our main question would be if the current automated probe- and laser annealing system can be upgraded to perform selective anti-aging.

- **Software improvements**. As a personal suggestion, the software stack comprises of a combination of Labview and Python. Both are used for their intended purposes, where Python is predominantly used to store data and to enable backend functionalities, while Labview is used for fast communication to control hardware and the user interface. One major flaw is the lack of version control and test coverage on the Labview side. This makes it difficult to study performance and reliability. The suggestion is to allocate time and resources in phasing-out Labview and replacing it by a complete Python package. This improves testability and allows more developers to take part in development.

6 Conclusion

Superconducting transmon devices are among the most mature architectures for realizing fault tolerant quantum processors utilizing logical qubits. With well developed error correction protocols, such as the QuSurf architecture, the need for precise frequency targeting of transmon qubits becomes apparent. Realizing this level of accuracy during device fabrication remains to be a challenge. This project therefore focuses on the realization of a post-fabrication method that fine-tunes the normal-state resistance of Josephson junctions using laser annealing to improve frequency targeting.

To reach this objective, a fully automated probe- and laser annealing station is developed. This includes: thoroughly tested control software, flexible user interface, certified laser safety enclosure and the algorithm responsible for active-feedback annealing. Beside these major components, a number of smaller addons have been created to ease the integration into the main fabrication pipeline.

The automated probing station utilizes a 4-point setup to measure junction conductance (resistance). The observed average deviation in conductance measured is 0.05% for a junction population between 100-300 μS. The observed average contribution of contact resistance to the junction-pair conductance is 4μS. The laser annealing setup succeeded in performing controlled junction resistance tuning. Either using an open-loop approach where junctions experience a fixed amount of thermal exposure, or using an active-feedback approach which iteratively tunes the junction resistance towards are target resistance. The maximum tunability range achieved is 12%. This is by no means the upper limit of the system. The observed targeting precision is $\leq 0.4\%$. The active-feedback algorithm is biased towards undershooting the target resistance, meaning that the average targeting precision is 0.2%. At an average qubit frequency of 6 GHz, this would translate to a deviation of 12 MHz in frequency. Well in range of the sub-50 MHz objective.

Unfortunately due to delivery delays during the pandemic, it was not possible to test the frequency targeting on a previously characterized surface-17 device. Nor was it possible quantify the effect on T_1 relaxation times. Both these characterizations and a further study in bi-directional annealing would make excellent research projects.

References

[1]N. Gisin et al. "Quantum cryptography". In: *Reviews of modern physics* 74.1 (2002), p. 145.

[2]P.W. Shor. "Polynomial-time algorithms for prime factorization and discrete logarithms on a quantum computer". In: *SIAM review* 41.2 (1999), pp. 303–332.

[3]D. Deutsch and R. Jozsa. "Rapid solution of problems by quantum computation". In: *Proceedings of the Royal Society of London. Series A: Mathematical and Physical Sciences* 439.1907 (1992), pp. 553–558.

[4]L.K. Grover. "Quantum computers can search arbitrarily large databases by a single query". In: *Physical review letters* 79.23 (1997), p. 4709.

[5]E.J. Zhang et al. "High-fidelity superconducting quantum processors via laser-annealing of transmon qubits". In: *arXiv preprint arXiv:2012.08475* (2020).

[6]F. Arute et al. "Quantum supremacy using a programmable superconducting processor". In: *Nature* 574.7779 (2019), pp. 505–510.

[7]D.P. DiVincenzo. "The physical implementation of quantum computation". In: *Fortschritte der Physik: Progress of Physics* 48.9-11 (2000), pp. 771–783.

[8]A.G. Fowler et al. "Surface codes: Towards practical large-scale quantum computation". In: *Physical Review A* 86.3 (2012), p. 032324.

[9]R. Versluis et al. "Scalable quantum circuit and control for a superconducting surface code". In: *Physical Review Applied* 8.3 (2017), p. 034021.

[10]D. Gottesman. "Stabilizer codes and quantum error correction". In: *arXiv preprint quant-ph/9705052* (1997).

[11]C. Huang et al. "Alibaba cloud quantum development platform: Surface code simulations with crosstalk". In: *arXiv preprint arXiv:2002.08918* (2020).

[12]M. Sarovar et al. "Detecting crosstalk errors in quantum information processors". In: *Quantum* 4 (2020), p. 321.

[13]P. Mundada et al. "Suppression of qubit crosstalk in a tunable coupling superconducting circuit". In: *Physical Review Applied* 12.5 (2019), p. 054023.

[14]M. Elliott, J. Joo, and E. Ginossar. "Designing Kerr interactions using multiple superconducting qubit types in a single circuit". In: *New Journal of Physics* 20.2 (2018), p. 023037.

[15]C. Granata et al. "Localized laser trimming of critical current in niobium based Josephson devices". In: *Applied physics letters* 90.23 (2007), p. 232503.

[16]J.B. Hertzberg et al. "Laser-annealing Josephson junctions for yielding scaled-up superconducting quantum processors". In: *arXiv preprint arXiv:2009.00781* (2020).

[17]N. Muthusubramanian et al. "Local trimming of transmon qubit frequency by laser annealing of Josephson junctions". In: *APS March Meeting Abstracts*. Vol. 2019. 2019, B29–015.

[18]M. Tinkham. *Introduction to superconductivity*. Courier Corporation, 2004, p. 15.

[19]J. Koch et al. "Charge-insensitive qubit design derived from the Cooper pair box". In: *Physical Review A* 76.4 (2007), p. 042319.

[20]J.J. Garcı´a-Ripoll, A. Ruiz-Chamorro, and E. Torrontegui. "Quantum Control of Frequency-Tunable Transmon Superconducting Qubits". In: *Physical Review Applied* 14.4 (2020), p. 044035.

[21]V. Bouchiat et al. "Quantum coherence with a single Cooper pair". In: *Physica Scripta* 1998.T76 (1998), p. 165.

[22]N.K. Langford et al. "Experimentally simulating the dynamics of quantum light and matter at deep-strong coupling". In: *Nature communications* 8.1 (2017), pp. 1–10.

[23]M.D. Hutchings et al. "Tunable superconducting qubits with flux-independent coherence". In: *Physical Review Applied* 8.4 (2017), p. 044003.

[24]D.J. Griffiths and D.F. Schroeter. *Introduction to quantum mechanics*. Cambridge University Press, 2018.

[25]V. Kasirajan. "The Quantum Superposition Principle and Bloch Sphere Representation". In: *Fundamentals of Quantum Computing*. Springer, 2021, pp. 75–104.

[26]R. Kleiner et al. "Superconducting quantum interference devices: State of the art and applications". In: *Proceedings of the IEEE* 92.10 (2004), pp. 1534–1548.

[27]J.D. Strand et al. "First-order sideband transitions with flux-driven asymmetric transmon qubits". In: *Physical Review B* 87.22 (2013), p. 220505.

[28]M.H. Devoret, A. Wallraff, and J.M. Martinis. "Superconducting qubits: A short review". In: *arXiv preprint cond-mat/0411174* (2004), p. 10.

[29]N.C. Jones et al. "Layered architecture for quantum computing". In: *Physical Review X* 2.3 (2012), p. 031007.
[30]S.B. Bravyi and A.Y. Kitaev. "Quantum codes on a lattice with boundary". In: *arXiv preprint quant-ph/9811052* (1998).
[31]L. DiCarlo et al. "Demonstration of two-qubit algorithms with a superconducting quantum processor". In: *Nature* 460.7252 (2009), pp. 240–244.
[32]R. Barends et al. "Superconducting quantum circuits at the surface code threshold for fault tolerance". In: *Nature* 508.7497 (2014), pp. 500–503.
[33]M.A. Rol et al. "Fast, high-fidelity conditional-phase gate exploiting leakage interference in weakly anharmonic superconducting qubits". In: *Physical review letters* 123.12 (2019), p. 120502.
[34]V. Ambegaokar and A. Baratoff. "Tunneling between superconductors". In: *Physical Review Letters* 10.11 (1963), p. 486.
[35]J. Ku et al. "Suppression of Unwanted ZZ Interactions in a Hybrid Two-Qubit System". In: *Physical review letters* 125.20 (2020), p. 200504.
[36]M. Ganzhorn et al. "Benchmarking the noise sensitivity of different parametric two-qubit gates in a single superconducting quantum computing platform". In: *Physical Review Research* 2.3 (2020), p. 033447.
[37]M. Kounalakis et al. "Tuneable hopping and nonlinear cross-Kerr interactions in a high-coherence superconducting circuit". In: *npj Quantum Information* 4.1 (2018), pp. 1–7.
[38]K.X. Wei et al. "Quantum crosstalk cancellation for fast entangling gates and improved multi-qubit performance". In: *arXiv preprint arXiv:2106.00675* (2021).
[39]M.A. Rol. "Control for Programmable Superconducting Quantum Systems". PhD Dissertation. Delft University of Technology, 2020. ISBN: 978-90-8593-451-6. URL: https://doi.org/10.4233/uuid:0a2ba212-f6bf-4c64-8f3d-b707f1e44953.
[40]Y.A. Kravtsov and Y.I. Orlov. "Limits of applicability of the method of geometric optics and related problems". In: *Soviet Physics Uspekhi* 23.11 (1980), p. 750.
[41]D. Wright et al. "Laser beam width, divergence and beam propagation factor—an international standardization approach". In: *Optical and quantum electronics* 24.9 (1992), S993–S1000.
[42]R. Paschotta. *M2 factor, explained by RP Photonics Encyclopedia; ISO Standard 11146.* https://www.rp-photonics.com/m2_factor.html. (Accessed on 10/06/2021).
[43]J.M. Kreikebaum et al. "Improving wafer-scale Josephson junction resistance variation in superconducting quantum coherent circuits". In: *Superconductor Science and Technology* 33.6 (2020), 06LT02.
[44]P.J. Koppinen, L.M. Väistö, and I.J. Maasilta. "Complete stabilization and improvement of the characteristics of tunnel junctions by thermal annealing". In: *Applied physics letters* 90.5 (2007), p. 053503.
[45]A. Bilmes et al. "In-situ bandaged Josephson junctions for superconducting quantum processors". In: *arXiv preprint arXiv:2101.01453* (2021).
[46]H. Scherer et al. "The effect of thermal annealing on the properties of Al–AlO x–Al single electron tunneling transistors". In: *Journal of Applied Physics* 90.5 (2001), pp. 2528–2532.

7 Appendix

7.1 Measurement Statistics

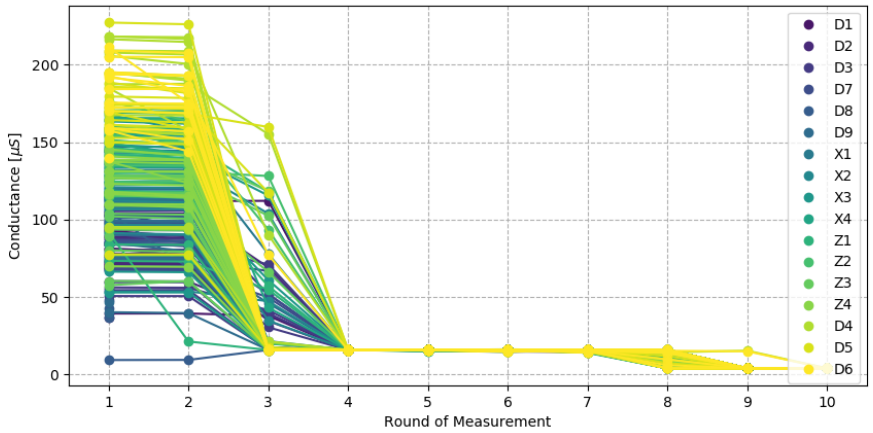

(a) Parallel

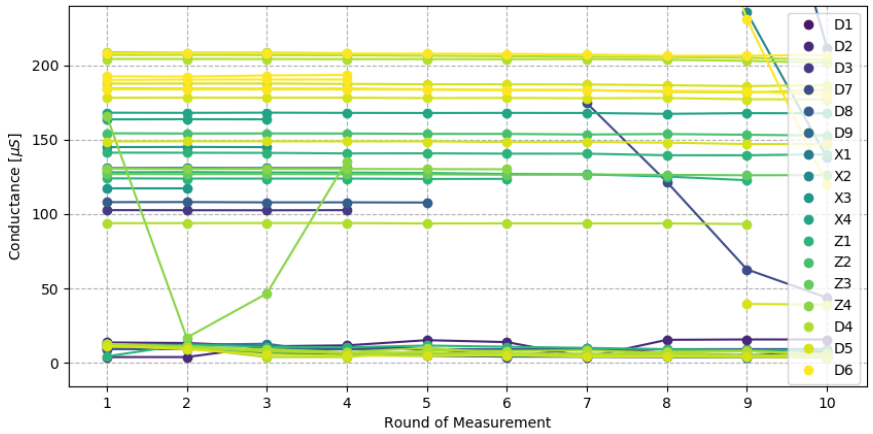

(b) Series

Figure 28: Junction-pair characterization statistics for a Blackbird device. Measurement order is based on a uniform random distribution. Using a **2-point** conductance measurement setup. (**Without** Z-stage calibration). (a) Each junction-pair is measured once before continuing to the next round. (b) Each junction-pair is measured 10-times before continuing to the next junction. A clear discrepancy in measurement values can be observed after x-amount of measurements, independent of the measurement technique used (parallel or series).

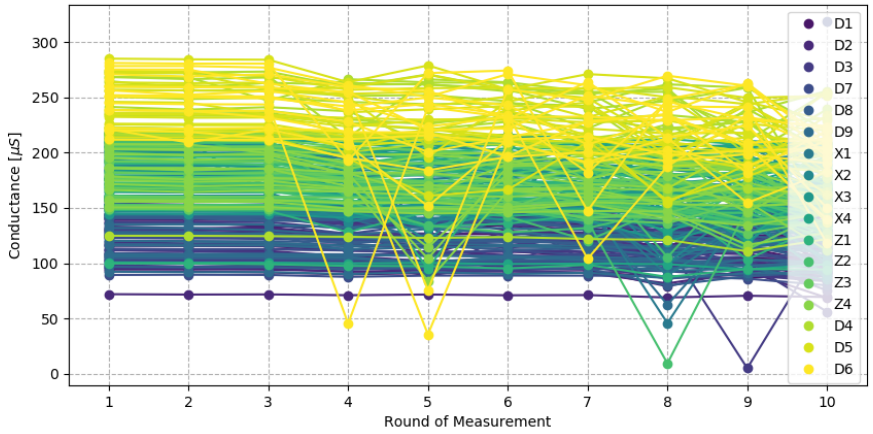

(a) Parallel

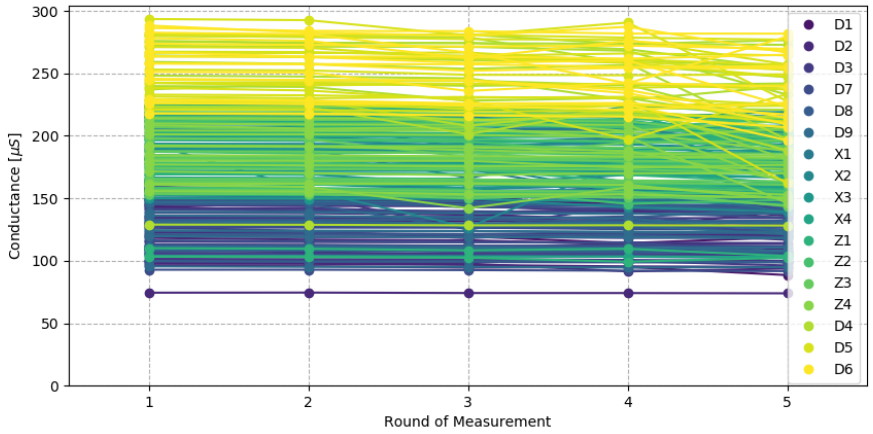

(b) Series

Figure 29: Junction-pair characterization statistics for a Blackbird device. Measurement order is based on a uniform random distribution. Using a **2-point** conductance measurement setup. (**With** Z-stage calibration). (a) Each junction-pair is measured once before continuing to the next round. (b) Each junction-pair is measured 10-times before continuing to the next junction. The vertical stage calibration improves the overall reliability of measurements for multiple successive rounds. Figure (b) is only performed up till round 5 since, looking back, this was enough to quantify the performance.

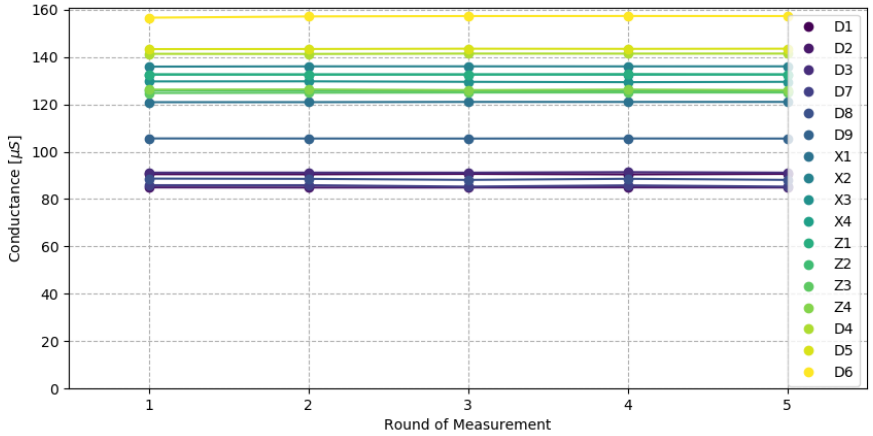

(a)

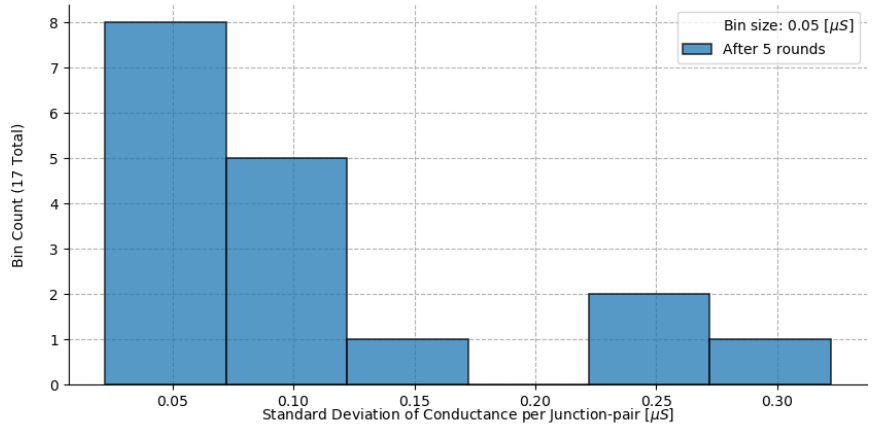

(b)

Figure 30: Junction-pair characterization statistics for a surface-17 device. Measurement order is based on a uniform random distribution. Using a **4-point** conductance measurement setup. (**With** Z-stage calibration). (a) Each junction-pair is measured once before continuing to the next round. (b) A histogram showing the standard deviation in conductance measured per junction-pair. The optimized system is able to achieve an average standard deviation in conductance of 0.13μS.